Thermodynamic Investigation of the Effect of Interface Curvature on Solid–liquid Equilibrium and Its Application to Zinc–air Battery Electrolyte at Low Temperature

by

Fanghui Liu

A thesis submitted in partial fulfillment of the requirements for the degree of

Master of Science

in

CHEMICAL ENGINEERING

Department of Chemical and Materials Engineering
University of Alberta

Abstract

Micro and nanoscale confinements and local curvatures, which are ubiquitous in natural and man-made materials and systems, cause significant impact on thermodynamic phase behavior. This effect has been extensively studied for single component solid–liquid phase transitions, but rarely for multicomponent systems. Using Gibbsian thermodynamics, we derived an expression to describe the thermodynamic solid–liquid equilibrium for multicomponent systems, where the equation takes thermal, mechanical and chemical equilibrium conditions into account. This derivation highlights the equivalence of general forms of the Gibbs–Thomson and Ostwald–Freundlich equations. We show the effect of the radius of curvature of the solid–liquid interface on the phase diagram, where the equation can be applied to the entire composition range. The equation can predict the effect of curvature on both the freezing and precipitating processes, thus a precise expression for the curvature-induced eutectic point shift is also derived. The water/glycerol system, which has complete mixing of the two components in the liquid phase but nearly pure solid phases during freezing and precipitating processes, is chosen to explore these equations. Here, we predict the curvature effect on the freezing and precipitating process of the entire phase diagram, and the eutectic point temperature and concentration shift with curvature. We also applied the equations to the freezing behavior of the aqueous electrolytes that are actively used in zinc–air batteries. The osmotic virial equation is an accurate, straightforward way to describe the nonideality of aqueous solution as a function of concentrations. Here, osmotic virial coefficients of various electrolytes which are commonly used are found by fitting literature data, and the nanoscale confinement effect on the freezing point of electrolyte systems is also investigated. The theoretical studies in this thesis, which used thermodynamic analysis to

investigate the nanoscale confinement effect on multicomponent solid–liquid equilibrium systems, can find crucial applications in cryobiology, soil science, synthetic nanoporous materials and other various nanoscience fields.

Preface

(Mandatory due to collaborative work)

This thesis is organized in four chapters.

Chapter 1 is the introduction.

Chapter 2 of this thesis, with minor modifications, has been published as: F. Liu, L. Zargarzadeh, H. J. Chung, and J. A. W. Elliott, "Thermodynamic investigation of the effect of interface curvature on solid–liquid equilibrium and eutectic point of binary mixtures", *Journal of Physical Chemistry B*, **2017**, *121* (40), pp 9452–9462. In Chapter 2, the Margules model coefficients for the water/glycerol system assuming a flat solid–liquid interface were found by Leila Zargarzadeh. This part of work was deleted from this thesis. Along with my supervisors, Leila also contributed to revising my original draft.

Chapter 3 of this thesis, has been prepared for submission as F. Liu, H. J. Chung and J. A. W Elliott, "Freezing of aqueous electrolytes in zinc–air batteries: Effect of composition and nanoscale confinement".

The overall conclusions of the thesis are summarized in Chapter 4.

Acknowledgements

I express my sincere gratitude wholeheartedly to both of my supervisors, Dr. Janet A.W. Elliott and Dr. Hyun-Joong Chung. Many people spend years to find a good mentor. I am so so lucky to have two. I would like to thank Dr. Elliott for her great enthusiasm, precious guidance, constant encouragement, and immense patience. She is a great female role model and gave me a lot of advice in life. I would like to thank Dr. Chung for his continuous care, enduring support, and kind encouragement.

I was fortunate to have great groupmates during my master's study at the University of Alberta. They made my two years of life in Canada fulfilling and they helped me a lot in both academic fields and life. I am especially appreciative of Nadia Shardt, Leila Zargarzadeh, and Li Liu. Thanks for the help in doing research and above all for precious friendship.

I wish to express my great love and gratitude to my beloved family: To my mother, Yanyan Dong, and my father, Shuangnan Liu, for their endless love, unconditional support, encouragement, and always being there for me.

I would also like to convey thanks to every individual who helped in the realization of this thesis, and thanks for everyone I met in Canada.

Fanghui Liu

December 2017

Table of Contents

List of Tables

List of Figures

List of Symbols

Nomenclature

θ	Contact angle
T	Temperature
P	Pressure
S	Entropy
s	Molar entropy
V	Volume
v	Molar volume
U	Internal energy
N	Number of moles
μ	Chemical potential
A	Area of the interface
σ	Interfacial tension
h	Spherical cap height
$\tilde{\pi}$	Osmole fraction
Π	Osmotic pressure
a	Activity
γ	Activity coefficient
R	Universal gas constant, 8.314 J/(mol K)
ΔH_1^{fus}	Molar enthalpy of fusion (latent heat of melting) for pure component 1
x	Mole fraction
$b_g, b_w, c_g, c_w, A_{wg}, A_{gw}$	Margules model coefficients
k_i^*	Mole-fraction-based dissociation constant of solute *i*
B_{ii}^*	Second mole-fraction-based osmotic virial coefficient of solute *i* (unitless)

C^*_{iii}	Third mole-fraction-based osmotic virial coefficient of solute *i* (unitless)
M	Molar mass

Superscripts

S	Solid phase
L	Liquid phase
SC	Solid–capillary interface
LC	Liquid–capillary interface
SL	Solid–liquid interface
res	Reservoir
sph	Spherical cap

Subscripts

m	Melting
1	Component 1, molecules that are present in both solid and liquid phase, water molecule
2	Glycerol molecule
F	Freezing process
P	Precipitating process
E	Eutectic point
w	Water
g	Glycerol

1. Introduction

1.1. Background

In surface chemistry and physics, different equations have been derived to show the effect of curved phase boundaries on the equilibrium. The role of curved phase boundaries is increasingly important for micro/nanoscale systems. The most well-known equation describing the impact of phase-boundary curvature on phase equilibrium is the Kelvin equation, which is the basis of all following studies. The original Kelvin equation was revised to represent combining chemical potential equilibrium with mechanical equilibrium,[1] and this form of the Kelvin equation can be extended to vapor–liquid equilibrium and liquid–liquid equilibrium. The Gibbs–Thompson equation and the Ostwald–Freundlich equation are two analogues of the Kelvin equation for solid–liquid equilibrium. The Gibbs–Thompson equation describes the equilibrium melting point of a small pure solid in its own pure liquid as a function of solid radius of curvature. The Ostwald–Freundlich equation expresses the solubility of a solid particle in a bulk liquid solution as a function of solid radius of curvature. The conditions for solid–liquid equilibrium include conditions for thermal, mechanical and chemical equilibrium, conditions that have been commonly applied in thermodynamic calculations. However, Gibbsian thermodynamics of composite systems utilizing knowledge of geometry has not been previously fully applied to provide the complete conditions for solid–liquid equilibrium of a solution confined in a pore made of a third non-soluble material. In addition, the most nonideal form of the Gibbs–Thompson equation and Ostwald–Freundlich equations have not been derived with the effect of contact angle. Most solid–liquid phase diagrams in literature consider only computations for a flat solid–liquid interface or if they do consider a curved solid–liquid interface, consider only a

narrow range of concentrations. To our knowledge, a rigorous thermodynamic study on the curvature effects for solid–liquid equilibrium in multicomponent systems has not been done over the complete range of concentrations and temperatures, nor has the effect of curvature on the eutectic point temperature and concentration been explored.

One of the applications of multicomponent liquid systems that may undergo freezing at low temperatures are alkali hydroxide aqueous electrolytes that are frequently used in secondary batteries for energy grid storage, where high specific energy, low material cost and environmental friendliness are keys for application. Understanding the freezing properties of aqueous electrolytes in secondary batteries is of vital importance for operations in cold climates. Ice crystal growth can break the structure, lower the conductivity and cause irreversible damage to the entire battery system. In such batteries where nanopores are abundant in electrodes, the nanopore can lower the freezing point of the system.[2] So investigation of the freezing point of multisolute aqueous electrolyte systems under confinement in the porous structure of the electrodes is necessary. Despite its importance for low-temperature operations, there is no prior work in literature that provides the freezing point change due to geometrical confinement of the electrolyte over a range of compositions and concentrations for various electrolytes and additives. A thermodynamic model that can predict how much ice is formed at a given temperature can be informative for engineers that design batteries for low temperature applications.

This thesis on nanoscale confinement effects on solid–liquid equilibrium gives a promising theoretical framework for solid–liquid equilibrium for multicomponent systems. These thermodynamic models can be applied in many fields such as cryobiology, forestry, soil science, and design of secondary batteries with aqueous electrolytes.

1.2. Scope of the thesis

This thesis is aimed to theoretically predict the thermodynamic properties of solid–liquid equilibrium of aqueous solutions confined in nanoscale pores. The thesis is investigated under the conditions of constant reference pressure ($P^L = 1$ atm), and negligible gravitational effects. The solid surfaces of pores are considered to be smooth, rigid, homogenous and nonsoluble in the solution confined within. The systems are liquid that can solidify confined in a capillary or pore with different radii. The interfacial tension of the solid–liquid interface is assumed to be a constant number, independent of temperature and concentration.

Chapter 2 gives the full derivation of the conditions for solid–liquid equilibrium, yielding the equilibrium temperature equation as a function of concentration and radius of curvature of the solid–liquid interface so that curvature effects on the phase diagram and eutectic point can be investigated.

Chapter 3 applies the equation derived in Chapter 2 to zinc–air battery electrolyte and investigates the confinement effect on freezing point depression for single solute electrolytes and electrolytes with additives.

The overall conclusions of the thesis are summarized in Chapter 4.

Throughout the thesis research, MATLAB was used for computational purposes and OriginsPro 8 was used for graph production.

2. Thermodynamic Investigation of the Effect of Interface Curvature on Solid–Liquid Equilibrium and Eutectic Point of Binary Mixtures

2.1. Abstract

Thermodynamic phase behavior is affected by curved interfaces in micro and nanoscale systems. For example, capillary freezing point depression is associated with the pressure difference between the solid and liquid phases caused by interface curvature. In this study, the thermal, mechanical and chemical equilibrium conditions are derived for binary solid–liquid equilibrium with a curved solid–liquid interface due to confinement in a capillary. This derivation shows the equivalence of the most general forms of the Gibbs–Thomson and Ostwald–Freundlich equations. As an example, the effect of curvature on solid–liquid equilibrium is explained quantitatively for the water/glycerol system. Considering the effect of a curved solid–liquid interface, a complete solid–liquid phase diagram is developed over a range of concentration for the water/glycerol system (including the freezing of pure water or precipitation of pure glycerol depending on the concentration of the solution). This phase diagram is compared with the traditional phase diagram in which the assumption of a flat solid–liquid interface is made. We show the extent to which nanoscale interface curvature can affect the composition-dependent freezing and precipitating processes, as well as the change in the eutectic point temperature and concentration with interface curvature. Understanding the effect of

curvature on solid–liquid equilibrium in nanoscale capillaries has applications in the food industry, soil science, cryobiology, nanoporous materials and various nanoscience fields.

2.2. Introduction

2.2.1. Effect of phase boundary curvature on phase diagrams

Understanding the fundamental science of solid, liquid or vapor confined in capillaries or pores is significant in surface chemistry and physics. Different equations have been proposed to explain the effect of phase boundary curvature on equilibrium. One of the most well-known equations is the Kelvin equation that describes the equilibrium vapor pressure above a curved interface compared to the vapor pressure above a flat interface at the same temperature. The initial equation derived by Lord Kelvin[3] was only approximate. It was not thermodynamically correct as it did not consider chemical potential equilibrium.[1] In the corrected form of the Kelvin equation, the mechanical equilibrium (Laplace equation) is combined with chemical potential equilibrium.[4,5] The Kelvin equation can be applied to drops, bubbles, and capillary-held wetting liquid menisci, and it has been validated for surfaces with mean radius of curvature larger than eight times the molecular diameter of the material of interest (for example for cyclohexane the Kelvin equation is valid down to a radius of curvature of 4 nm).[6,7] Later on, several groups extended the Kelvin equation to multicomponent mixtures in vapor–liquid equilibrium,[8,9] taking into account chemical potential equilibrium for multiple components in different phases, *i.e.,* equality of chemical potential of each component in different phases.[10] Although the Kelvin equation was initially derived for the case of vapor–liquid equilibrium, the idea can be extended to liquid–liquid equilibrium. The liquid–liquid analogue of the Kelvin equation has been applied

to investigate the thermodynamic equilibrium of micro and nanodrops being concentrated by partial dissolution into a surrounding oil phase.[11,12]

The Gibbs–Thompson equation is an analogue of the Kelvin equation for solid–liquid equilibrium that describes the equilibrium melting point of a small pure solid crystal in its own pure liquid as a function of crystal radius. The validity of the Gibbs–Thompson equation has been proven by experiments.[13,14] There are many experiments showing the effect of curvature on phase equilibrium in a range of porous systems: metal oxide gels, porous glasses and nanoporous materials.[15] For single component solid–liquid equilibrium confined inside pores, the experimental results have been compared with theoretical predictions to show the relevance of the size of the pores.[16,17] The capillary freezing point inside glass capillaries with radii of 3 μm to 87 μm was measured while the image of the ice–solution interface was captured to analyze the contact angle.[14] For porous materials with different nanoscale curvature in single component solid–liquid equilibrium, the freezing temperature of liquid in a pore is lower than that of bulk liquid with a flat surface. The Gibbs–Thompson equation has been shown to be valid to predict the freezing and melting point depression of ice in nanoscopic glass pores that are as small as ~4 nm in diameter.[18] The Gibbs–Thompson equation can also be extended for multicomponent systems in solid–liquid equilibrium. In cryobiology, in which cells in solution or tissues are subjected to low temperatures, the temperature at which ice propagates through confined spaces is lowered by the Gibbs–Thomson effect.[19,20,21] Also the Gibbs–Thomson equation has been applied to predict microstructure formation during solidification in multicomponent systems.[22]

The Ostwald–Freundlich equation is another analogue of the Kelvin equation for solid–liquid equilibrium. Introduced by Ostwald[23] and later corrected by Freundlich,[24] the Ostwald–Freundlich equation[25] expresses the solubility of a solid particle in a bulk liquid solution as a

function of particle curvature. As the size of the solids is decreased to the nanoscale, the solubility will depend on the size of the particle.[26] A nonideal form of the Ostwald–Freundlich equation developed by Eslami *et al.* was used to describe the effect of precipitate solute curvature on aqueous microdrop concentrating processes.[27]

The references mentioned above consider only the computation of the equilibrium state in a narrow range of concentration. Studies on the effect of curvature on phase equilibrium in multicomponent systems have been quite limited compared with single component systems. To our knowledge, a rigorous thermodynamic study has not been done of the effects of curvature on solid–liquid equilibrium in multicomponent systems over the complete range of concentration and temperature.

Some recent works studied the effect of curvature on multicomponent vapor–liquid equilibrium.[28,29] In nanosized pores in which vapor and liquid phases coexist, equation-of-state models have been used to describe capillary condensation for binary mixtures, and to calculate the critical pore radius, and condensed-phase equilibrium pressure for nanosized pores.[28,30] Another example by Shardt and Elliott is the investigation of the curvature effect on multicomponent vapor–liquid phase equilibrium. They developed phase envelopes and phase composition diagrams for the ideal system methanol/ethanol and the nonideal system ethanol/water. They showed that the azeotrope (equal volatility point in nonideal systems) shifts with nanoscale curvature.[29]

In the field of materials science, several studies attempted to model phase diagrams for nanoscale alloys by adding surface thermodynamic terms to the Gibbs free energy of bulk available in CALPHAD (CALculation of PHAse Diagram).[31,32] However, that approach is not

consistent with the Gibbsian thermodynamics of composite systems[1] which is the basis of the work presented here. That approach[31,32] does not lead to the well-known Gibbs–Thomson equation and Ostwald–Freundlich equations.

In this work we develop the effect of solid curvature on the solid–liquid phase diagram across the entire composition range for any arbitrary binary solution that forms pure solids including the effect of the contact angle at which the solid–liquid interface contacts a confining pore wall.

2.2.2. Solid–liquid phase diagrams in the absence of curvature

Solid–liquid phase diagrams can have many complexities. However, there are many multicomponent systems for which the solid phases are in pure form because of the differences in molecular size and/or molecular structure.[33] Partial miscibility of solid phases (resulting in non-pure solid phases) is uncommon in cases other than metallic systems.[34] Here, our focus is on aqueous solutions. For the purposes of this thesis, we restrict our discussion to binary systems in which a pure solid phase is in equilibrium with a solution. Such systems have only two possible solid phases and a single eutectic point.

An illustrative phase diagram in Figure 1 describes the phase behaviour of such a two-component mixture at constant pressure. At higher temperature, the solution exists as a single phase, *i.e.,* an unsaturated stable homogenous liquid phase. At lower temperature the liquid separates into a *pure* solid phase and a liquid solution. The component of the pure solid phase depends on the concentration of the liquid solution. If we choose one component to call the solvent and one to call the solute, the left part of Figure 1 is the freezing process of the solvent and the right part is the precipitating process of the solute.

Liquidus lines (curves *ae* and *be*) in Figure 1 represent the onset of solidification. In the case of an aqueous solution, curve *ae* shows the composition dependent freezing point depression, whereas the curve *eb* represents the concentration dependent solubility limit of the other component in the aqueous solution. The liquidus lines also show the concentration of the unfrozen or unprecipitated solution at a given temperature. The left and right liquidus meet at a minimum point *e*, called the eutectic ("easy melting") point.[34] The eutectic point is the point where solid solute, solid solvent and liquid mixture coexist. The eutectic point is the lowest temperature for the given pressure at which the liquid phase is stable. Below the eutectic point, the system consists of two pure solid phases. When a liquid solution of a given overall composition is cooled, the system temperature lowers at constant composition until a liquidus line is met and solidification begins, with further cooling the composition of the remaining liquid follows the liquidus line to the eutectic point.

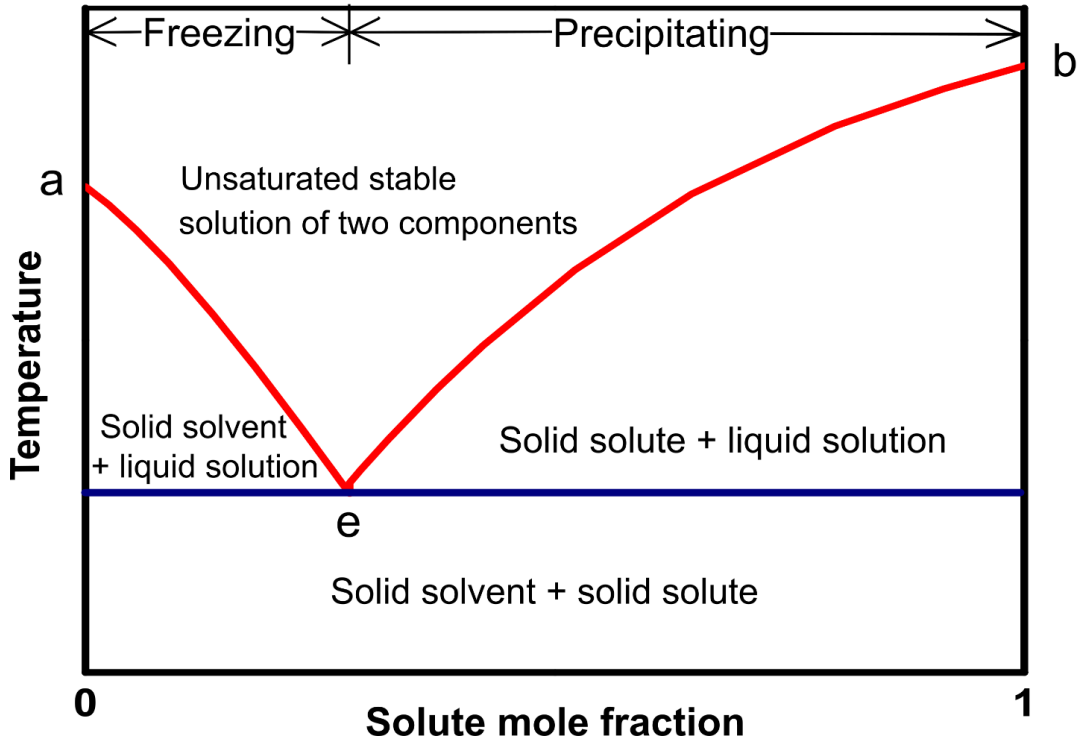

Figure 1. Illustrative constant pressure, temperature–composition phase diagram of solid–liquid equilibrium in a binary system with a simple eutectic and pure solid phases above the eutectic temperature.

2.2.3. Objectives of this work

The phase diagram shown in Figure 1 is constructed under the assumption that the interface between the solid and liquid is flat. In this thesis, we apply Gibbsian composite system thermodynamics to understand the effect of interface curvature on solid–liquid phase equilibrium in a binary mixture. We start by deriving the general conditions for solid–liquid equilibrium in a capillary which imposes a curved solid–liquid interface. The conditions for equilibrium are then examined for the case of the water/glycerol system, quantifying the effect of interface curvature on the two liquidus lines (freezing point temperature as a function of concentration and

precipitation saturation concentration as a function of temperature). The eutectic point temperature and concentration are also calculated. As an example to explore the effects of curvature, we chose the water/glycerol binary system, since this system exhibits complete miscibility in the liquid state and nearly complete insolubility between components in the respective solid states (*i.e.,* pure component solids). Furthermore, water/glycerol solid–liquid phase diagrams have important applications since glycerol is a popular antifreeze substance—the first permanent type antifreeze agent for radiator cooling systems in automobiles,[35] and the first cryoprotectant for preserving living cells.[36]

2.3. Governing Equations

2.3.1. Derivation of general conditions for solid–liquid equilibrium and calculating the liquidus lines (freezing and solute precipitation) and eutectic point

Gibbsian thermodynamics of composite systems gives a formal approach for finding the conditions for equilibrium of a multiphase multicomponent system by extremizing entropy subject to constraints on the system. Our objective is to find the effect of confinement in a capillary of radius r on the solid–liquid phase diagram of a two-component aqueous system. Here, the largest radius of curvature that a solid phase forming out of the aqueous solution can have is defined by the interaction with the capillary wall. Thus we consider the equilibrium of the system illustrated in Figure 2, where a single-component solid phase is in equilibrium with a two-component liquid phase and where the curved solid–liquid interface contacts the capillary wall at the contact angle, θ.

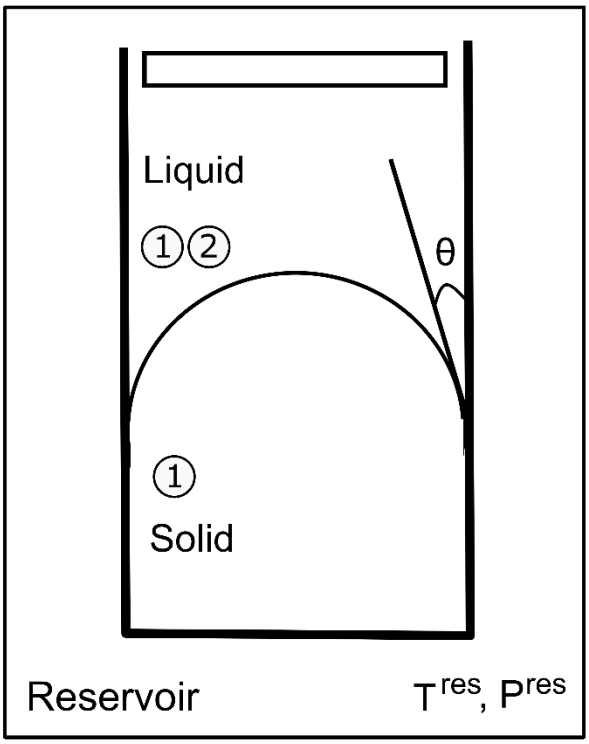

Figure 2. Schematic of solid–liquid equilibrium with a curved solid–liquid interface in a capillary.

We assign the solid components in the capillary wall to be part of the reservoir and assign the liquid–capillary and solid–capillary interfaces to be parts of the system.[1] The solid phase can be either pure ice or pure precipitated solute, as we limit our study only to those aqueous solutions in which ice forms as pure water or solute precipitates as pure solute. Component 1 represents the molecules that are in the solid phase and liquid phase and component 2 represents the other molecules that are in the liquid phase. The solid–liquid interface contains molecules of both components 1 and 2. The liquid–capillary and solid–capillary interfaces are considered to be part of the system so that adsorption of components 1 and 2 at the liquid–capillary and solid–capillary interfaces is included in consideration. The pressure and temperature of the reservoir surrounding the system (including the capillary solid), P^{res} and T^{res}, respectively, are considered to remain

constant. The system does not exchange any mass with the reservoir, therefore the number of molecules of each component in the system is constant. Molecules of component 1 are present in the solid phase (solid solvent or precipitate), the liquid phase (solvent/solute mixture), the solid–liquid interface, the liquid–capillary interface and the solid–capillary interface. Molecules of component 2 are present in the liquid phase, the solid–liquid interface and the liquid–capillary interface; however, they do not exist in the solid or the solid–capillary interface.

We can find the conditions for equilibrium of the system by finding the conditions that extremize entropy of the system plus reservoir:

$$dS = dS^S + dS^L + dS^{SC} + dS^{LC} + dS^{SL} + dS^{res} = 0 \tag{1}$$

where S^S, S^L and $S^{res}$are the entropies of the solid phase, the liquid phase and the reservoir, and S^{SC}, S^{LC}, S^{SL} are the entropies of the solid–capillary, liquid–capillary, and solid–liquid interfaces, respectively. The entropy differentials can be written as in Equations (2)–(7) using the fundamental relations and the definitions of intensive properties temperature T, pressure P, and chemical potential μ.[37] The differential of entropy of the liquid phase (superscript L) is written as:

$$dS^L = \frac{1}{T^L} dU^L + \frac{P^L}{T^L} dV^L - \frac{\mu_1^L}{T^L} dN_1^L - \frac{\mu_2^L}{T^L} dN_2^L \tag{2}$$

where V is volume, U is internal energy, μ_i^L is the chemical potential of component i in the liquid phase and N_i^L is the number of moles of component i in the liquid phase. Since component 2 does not exist in the solid phase, the differential of entropy of the solid phase (superscript S) is written as:

$$dS^S = \frac{1}{T^S} dU^S + \frac{P^S}{T^S} dV^S - \frac{\mu_1^S}{T^S} dN_1^S \quad (3)$$

Using Gibbs Surface of Tension approach, the curved solid–liquid interface (superscript *SL*) is treated as a phase that has area but no volume and to which are assigned excess properties (S^{SL}, U^{SL}, N_1^{SL}, N_2^{SL}) and an interfacial tension σ, the value for which does not depend explicitly on curvature. Therefore, the differential of the solid–liquid interface entropy is given by

$$dS^{SL} = \frac{1}{T^{SL}} dU^{SL} - \frac{\sigma^{SL}}{T^{SL}} dA^{SL} - \frac{\mu_1^{SL}}{T^{SL}} dN_1^{SL} - \frac{\mu_2^{SL}}{T^{SL}} dN_2^{SL} \quad (4)$$

where A is the area of the interface, μ_1^{SL} represents the chemical potential of surface excess component 1 molecules, and σ^{SL} represents the solid–liquid interfacial tension.

Since the radius of the capillary will not be changing as the system evolves to equilibrium, it is convenient to adopt the Gibbs Dividing Surface approach in which the dividing surfaces between the capillary and either the liquid or solid phases are placed such that there are no excess moles of the capillary solid material in the interfaces. We will be either leaving the contact angle as a variable or setting the contact angle, hence we will not have to explicitly introduce any curvature dependence for the interfacial tension of the capillary solid and therefore proceed without loss of generality. This is also consistent with defining the reservoir to contain all molecules of the capillary solid. Therefore, the differential of the entropy of the liquid–capillary interface (superscript *LC*) is:

$$dS^{LC} = \frac{1}{T^{LC}} dU^{LC} - \frac{\sigma^{LC}}{T^{LC}} dA^{LC} - \frac{\mu_1^{LC}}{T^{LC}} dN_1^{LC} - \frac{\mu_2^{LC}}{T^{LC}} dN_2^{LC} \quad (5)$$

and the differential of the entropy of the solid–capillary interface (superscript *SC*) is:

$$dS^{SC} = \frac{1}{T^{SC}} dU^{SC} - \frac{\sigma^{SC}}{T^{SC}} dA^{SC} - \frac{\mu_1^{SC}}{T^{SC}} dN_1^{SC} \tag{6}$$

Finally, the differential of the entropy of the reservoir (superscript *res*) may be written:

$$dS^{res} = \frac{1}{T^{res}} dU^{res} + \frac{P^{res}}{T^{res}} dV^{res} - \frac{\mu^{res}}{T^{res}} dN^{res} \tag{7}$$

Next the system constraints are enumerated. The total internal energy of the system plus reservoir is constant:

$$dU^{res} = -dU^{S} - dU^{L} - dU^{SL} - dU^{SC} - dU^{LC} \tag{8}$$

The total volume of the system plus reservoir is constant:

$$dV^{res} = -dV^{S} - dV^{L} \tag{9}$$

The total number of moles of component 1 in the system (solid phase, liquid phase, solid–liquid interface, solid–capillary interface, and liquid–capillary interface) is constant:

$$dN_1^{S} = -dN_1^{L} - dN_1^{SL} - dN_1^{SC} - dN_1^{LC} \tag{10}$$

The total number of moles of component 2 in the system (liquid phase, liquid–capillary interface, and solid–liquid interface) is constant:

$$dN_2^{L} = -dN_2^{SL} - dN_2^{LC} \tag{11}$$

The number of moles in the reservoir is also constant.

$$dN^{res} = 0 \tag{12}$$

The next step is to use geometric knowledge to impose relationships between phase volumes and areas since changes in these are not independent. We assume that the solid–liquid interface takes the shape of a spherical cap with geometry as defined in Figure 3.

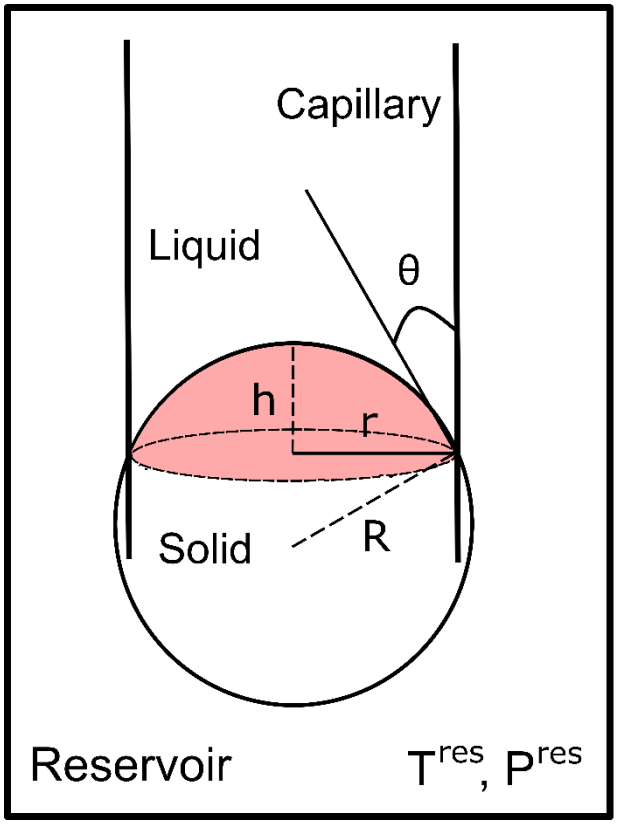

Figure 3. Schematic diagram of the geometry of solid–liquid equilibrium in a capillary. The solid–liquid interface is assumed to take the shape of a spherical cap with height *h* and base width equal to the capillary radius *r*. The radius of curvature of the solid–liquid interface is *R*.

Denoting the surface area of the spherical cap A_{cap}^{sph}, and the volume of the spherical cap V_{cap}^{sph}, the following geometrical relationships are valid.[38]

$$A_{cap}^{sph} = 2\pi Rh = \frac{2\pi r^2(1-sin\theta)}{cos^2\theta} \tag{13}$$

$$V_{cap}^{sph} = \frac{\pi h(3r^2+h^2)}{6} = \frac{\pi r^3(sin^3\theta - 3sin\theta + 2)}{3cos^3\theta} \tag{14}$$

$$R = \frac{r}{cos\theta} = \frac{h}{1-sin\theta} \tag{15}$$

The increase in the liquid–capillary area equals the decrease in the solid–capillary area:

$$dA^{LC} = -dA^{SC} \tag{16}$$

The change in the area of the solid–liquid interface can be found by taking the derivative of Equation (13).

$$dA^{\mathrm{SL}} = dA_{cap}^{sph} = \frac{4\pi r(1 - sin\theta)}{cos^2\theta}dr - \frac{2\pi r^2(sin\theta - 1)^2}{cos^3\theta}d\theta \tag{17}$$

The change in the volume of the solid can be found by realizing that the solid volume can be changed by changes in the volume of the spherical cap or by moving the spherical cap up or down in the capillary:

$$\begin{aligned} dV^S &= dV_{cap}^{sph} + \frac{1}{2}rdA^{SC} \\ &= \frac{1}{2}rdA^{SC} + \frac{\pi r^2(2 - 3sin\theta + sin^3\theta)}{cos^3\theta}dr - \frac{\pi r^3(sin\theta - 1)^2}{cos^4\theta}d\theta \end{aligned} \tag{18}$$

Substituting Equations (2)–(7) into Equation (1), making use of constraints in Equations (8)–(12), (16)–(18), noting that since the temperature and pressure of the reservoir are fixed, $dr = 0$, and collecting like terms yields:

$$\left(\frac{1}{T^L}-\frac{1}{T^{res}}\right)dU^L+\left(\frac{1}{T^S}-\frac{1}{T^{res}}\right)dU^S+\left(\frac{1}{T^{SL}}-\frac{1}{T^{res}}\right)dU^{SL}+\left(\frac{1}{T^{LC}}-\frac{1}{T^{res}}\right)dU^{LC} \quad (19)$$
$$+\left(\frac{1}{T^{SC}}-\frac{1}{T^{res}}\right)dU^{SC}+\left(\frac{\mu_1^L}{T^L}-\frac{\mu_1^{SC}}{T^{SC}}\right)dN_1^L+\left(\frac{\mu_1^S}{T^S}-\frac{\mu_1^{SC}}{T^{SC}}\right)dN_1^S$$
$$+\left(\frac{\mu_1^{SL}}{T^{SL}}-\frac{\mu_1^{SC}}{T^{SC}}\right)dN_1^{SL}+\left(\frac{\mu_1^{LC}}{T^{LC}}-\frac{\mu_1^{SC}}{T^{SC}}\right)dN_1^{LC}+\left(\frac{\mu_2^L}{T^L}-\frac{\mu_2^{LC}}{T^{LC}}\right)dN_2^L$$
$$+\left(\frac{\mu_2^L}{T^{SL}}-\frac{\mu_2^{LC}}{T^{LC}}\right)dN_2^{SL}+\left(\frac{P^L}{T^L}-\frac{P^{res}}{T^{res}}\right)dV^L$$
$$+\left[\frac{1}{2}r\left(\frac{P^S}{T^S}-\frac{P^{res}}{T^{res}}\right)+\left(\frac{\sigma^{LC}}{T^{LC}}-\frac{\sigma^{SC}}{T^{SC}}\right)\right]dA^{SC}$$
$$+\left[\left(\frac{P^S}{T^S}-\frac{P^{res}}{T^{res}}\right)\left(\frac{-\pi r^3(sin\theta-1)^2}{cos^4\theta}\right)-\frac{\gamma^{SL}}{T^{SL}}\left(\frac{-2\pi r^2(sin\theta-1)^2}{cos^3\theta}\right)\right]d\theta=0$$

After considering all constraints and geometrical relations, all differentials in Equation (19) are independent. So, for Equation (19) to be true for any possible variation about equilibrium, the coefficients multiplying the differentials in Equation (19) must each be set equal to zero, thus yielding the following conditions for equilibrium:

$$T^S=T^L=T^{SL}=T^{SC}=T^{LC}=T^{res}=T \quad (20)$$

$$\mu_1^S=\mu_1^L=\mu_1^{SL}=\mu_1^{SC}=\mu_1^{LC} \quad (21)$$

$$\mu_2^L=\mu_2^{SL}=\mu_2^{LC} \quad (22)$$

$$P^L=P^{res} \quad (23)$$

$$P^S-P^L=\frac{2\sigma^{SL}cos\theta}{r} \quad (24)$$

$$\sigma^{SC}-\sigma^{LC}=\sigma^{SL}cos\theta \quad (25)$$

Equation (20) is the thermal equilibrium condition. Equations (21) and (22) are chemical equilibrium conditions. Equation (23) is the mechanical equilibrium between the reservoir and

liquid phase. Equations (24) and (25) are also mechanical equilibrium conditions; Equation (24) is the Young–Laplace equation and Equation (25) is the Young equation.

By assuming the system temperature T and the liquid phase pressure P^L are set by the reservoir, the set of equilibrium conditions that arise from Equations (20)–(25) can be combined to calculate the liquidus lines. In Equation (24), when the solid–liquid interface is flat, r goes to infinity and the pressure in the solid phase is equal to the pressure in the liquid phase. It should be noted that the radius of curvature is defined to be positive when the center of the circle that defines the interface is placed inside the solid phase, *i.e.,* when the interface is curved towards the solid. We combine the thermal equilibrium (equality of temperature of the solid phase, liquid phase and solid–liquid interface), the mechanical equilibrium of Equations (23) and (24), and the equality of chemical potential of component 1 in the solid and liquid (the first equivalence in Equations (21)) to get,

$$\mu_1^L(T, P^L, x_1^L) = \mu_1^S(T, P^S) \tag{26}$$

To develop the governing equation for the phase diagram, Equation (24) and equations of state for the chemical potentials must be inserted into Equation (26). The chemical potential of the solidifying component in the pure solid phase can be found by assuming that the solid phase is incompressible and that the solid molar entropy is independent of temperature, and thus can be expressed by:

$$\mu_1^S(T, P^S) = \mu_1^S\left(T_{m,1}, P^L\right) - s_1^S\left(T - T_{m,1}\right) + v_1^S(P^S - P^L) \tag{27}$$

where $T_{m,1}$, the melting point of pure component 1 at the pressure of the bulk phase (*i.e.,* liquid phase pressure P^L), is chosen as the reference point for calculating chemical potential. s_1^S and v_1^S

are the molar entropy, and molar volume of pure component 1 in the solid phase at $T_{m,1}$ and P^L, respectively.

Before giving the chemical potential of component 1 in the liquid phase, we define auxiliary functions osmole fraction $\tilde{\pi}$, osmotic pressure Π, activity a and activity coefficient γ by their relationships to chemical potential in the liquid.[39,40,41]

$$\tilde{\pi} = -\frac{\mu_1^L - \mu_1^{L0}}{RT} \tag{28}$$

where μ_1^L is the chemical potential of component 1 in the liquid phase, μ_1^{L0} is the chemical potential of pure liquid component 1 and from here on R is the universal gas constant. The activity of component 1 in solution can be expressed:

$$a_1^L = x_1^L \gamma_1^L \tag{29}$$

where a_1^L is the composition-dependent activity of component 1 in the binary solution and γ_1^L is the composition-dependent activity coefficient of component 1 in solution which accounts for solution nonideality.

$$\Pi = \frac{RT\tilde{\pi}}{v_1^L} = -\frac{RT\ln(a_1^L)}{v_1^L} = -\frac{RT\ln(x_1^L \gamma_1^L)}{v_1^L} \tag{30}$$

where v_1^L is the molar volume of pure liquid component 1 and Π is binary solution composition-dependent osmotic pressure.

For the chemical potential of component 1 in the liquid solution, we use:

$$\mu_1^L(T, P^L, x_1^L) = \mu_1^{L0}\left(T_{m,1}, P^L\right) - s_1^L\left(T - T_{m,1}\right) + RT\ln(x_1^L \gamma_1^L) \tag{31}$$

where s_1^L is the temperature-independent molar entropy of pure component 1 in liquid form at $T_{m,1}$ and P^L.

The chemical potential can equivalently be expressed in terms of osmotic pressure.[21]

$$\mu_1^L(T, P^L, x_1^L) = \mu_1^{L0}(T_{m,1}, P^L) - s_1^L(T - T_{m,1}) - v_1^L \Pi(T, x_1^L) \tag{32}$$

Substituting Equations (27) and (31) into Equation (26), and replacing $(s_1^L - s_1^S)$ using the Clapeyron equation:

$$\frac{1}{s_1^L - s_1^S} = \frac{T_{m,1}}{\Delta H_1^{fus}} \tag{33}$$

where $\Delta H_1^{fus}$is the molar enthalpy of fusion (latent heat of melting) for pure component 1 at $T_{m,1}$ and P^L, leads to:

$$\ln(x_1^L \gamma_1^L) = \frac{\Delta H_1^{fus}}{R T_{m,1}} \left(1 - \frac{T_{m,1}}{T}\right) + \frac{v_1^S}{RT}(P^S - P^L) \tag{34}$$

Substituting the Laplace equation, Equation (24), for the pressure difference term in Equation (34) and rearranging for the solid–liquid equilibrium temperature yields:

$$T = \frac{\frac{2 v_1^S \sigma^{SL} cos\theta}{r} - \Delta H_1^{fus}}{R \ln(x_1^L \gamma_1^L) - \frac{\Delta H_1^{fus}}{T_{m,1}}} \tag{35}$$

The freezing or precipitating temperature depression can be expressed as:

$$T_{m,1} - T = \frac{R T_{m,1} \ln(x_1^L \gamma_1^L) - \frac{2 v_1^S \sigma^{SL} cos\theta}{r}}{R \ln(x_1^L \gamma_1^L) - \frac{\Delta H_1{}^{fus}}{T_{m,1}}} \tag{36}$$

Equation (36) is a very general form of both the Gibbs–Thomson equation and the Ostwald–Freundlich equation that also include the effect of the contact angle. The way we have done this derivation highlights the equivalence of the Gibbs–Thomson and Ostwald–Freundlich equations. Equation (35) and (36) are each nonideal forms of both the Gibbs–Thomson equation and Ostwald–Freundlich equation, the naming of the equation depending only on which component is identified as component 1.

Alternatively and more commonly for the freezing process than the precipitating process, the solidifying point depression can also be written in terms of osmotic pressure:

$$T_{m,1} - T = \frac{2v_1^S \sigma^{SL} T_{m,1} cos\theta}{r\Delta H_1^{fus}\left(1 + \frac{RT_{m,1}\tilde{\pi}}{\Delta H_1^{fus}}\right)} + \frac{\frac{R\tilde{\pi}T_{m,1}^2}{\Delta H_1^{fus}}}{1 + \frac{R\tilde{\pi}T_{m,1}}{\Delta H_1^{fus}}} \tag{37}$$

$$= \frac{2v_1^S \sigma^{SL} T_{m,1} cos\theta}{r\Delta H_1^{fus}} + \frac{v_1^L \Pi T_{m,1}}{\Delta H_1^{fus}}$$

The first term of Equation (37) is the capillary effect, and the second term of Equation (37) is the osmotic effect.[14] Equation (37) has an osmole fraction version and an osmotic pressure version. The osmotic pressure version can be found in previous work.[14,21] The second term of the osmole fraction version has been applied in multi–solute nonideal solutions without curvature effects.[42]

For a flat solid–liquid interface, the pressure of the solid phase equals the pressure in the liquid phase and $\frac{2v_1^S \sigma^{SL}}{r}$ in Equations (35)–(37) is zero. For a curved interface, the pressure difference between the solid and liquid phases varies as a function of the radius of curvature according to Equation (24) and the curvature term appears in Equations (35)–(37).

The freezing and precipitating liquidus lines meet at a minimum point which is called the eutectic point. In order to calculate the eutectic point concentration and temperature, we use T_F and T_P to represent the freezing temperature of solvent and the precipitating temperature of solute, respectively. Then according to Equation (35) for the solidifying temperature, and considering the fact that summation of mole fractions in liquid phase is 1 (hence for a binary system $x_{solvent}^{L} + x_{solute}^{L} = 1$)

$$T_F = \frac{\frac{2v_F^S\sigma_F^{SL}cos\theta_F}{r} - \Delta H_F^{fus}}{R\ln[(1-x_{solute}^{L})\gamma_F^{L}] - \frac{\Delta H_F^{fus}}{T_{m,F}}} \tag{38}$$

$$T_P = \frac{\frac{2v_P^S\sigma_P^{SL}cos\theta_P}{r} - \Delta H_P^{fus}}{R\ln(x_{solute}^{L}\gamma_P^{L}) - \frac{\Delta H_P^{fus}}{T_{m,P}}} \tag{39}$$

where x_{solute}^{L} is the mole fraction of solute in the liquid phase, v_F^S and v_P^S represent the molar volume of pure solvent solid phase in the freezing process and pure solute solid phase in the precipitating process, respectively. ΔH_F^{fus} and ΔH_P^{fus} represent the molar enthalpy of fusion of solvent in the freezing process and solute in the precipitating process. σ_F^{SL} and σ_P^{SL} represent the interfacial tensions of solid solvent–liquid solution in the freezing process and solid solute–liquid solution in the precipitating process, respectively. θ_F and θ_P represent the contact angle between the curved solid–liquid interface and the capillary in the freezing and precipitating process, respectively. γ_F^{L} and γ_P^{L} represent the activity coefficients of solvent in the liquid phase in the freezing process and solute in the liquid phase in the precipitating process, respectively. At the eutectic point, T_F equals T_P and equating Equations (38) and (39) yields an equation for the eutectic point solute concentration, x_E.

$$\frac{\frac{2v_F^S\sigma_F^{SL}cos\theta_F}{r}-\Delta H_F^{fus}}{R\ln[(1-x_E)\gamma_F^L]-\frac{\Delta H_F^{fus}}{T_{m,F}}}=\frac{\frac{2v_P^S\sigma_P^{SL}cos\theta_P}{r}-\Delta H_P^{fus}}{R\ln(x_E\gamma_P^L)-\frac{\Delta H_P^{fus}}{T_{m,P}}} \quad (40)$$

which can be solved together with Equation (35) for the eutectic temperature. It has already been noted in previous work that the eutectic point concentration equation for a binary system with a flat surface is usually a transcendental equation,[43] which is difficult to solve directly. So linear fitting[44] and polynomial fitting[45] are used. Here we give the transcendental equation for the eutectic solute concentration in the case of curved interfaces. Equation (40) can be solved numerically together with Equation (35) to yield the eutectic solute concentration and the eutectic temperature for a given curvature.

In order to present the maximum effect of curvature, and for lack of the required information to do otherwise, we take the contact angle that either the ice–liquid interface or the glycerol precipitate–liquid interface makes with the capillary solid wall to be zero for this exploration. Note that this is also equivalent to considering a nucleating sphere of either ice or precipitate without interaction with the capillary solid, the maximum radius of curvature of which equals the radius of the capillary. By setting the contact angle equal to zero, we have removed from our concern the role of adsorption at the capillary solid wall. For this work, the zero contact angle assumption may exaggerate the predicted freezing/precipitation point depression due to capillary radius. In the case of zero contact angle, Equation (35) becomes:

$$T=\frac{\frac{2v_1^S\sigma^{SL}}{r}-\Delta H_1^{fus}}{R\ln(x_1^L\gamma_1^L)-\frac{\Delta H_1^{fus}}{T_{m,1}}} \quad (41)$$

The freezing or precipitating temperature depression can be expressed as:

$$T_{m,1} - T = \frac{RT_{m,1}\ln(x_1^L\gamma_1^L) - \frac{2v_1^S\sigma^{SL}}{r}}{R\ln(x_1^L\gamma_1^L) - \frac{\Delta H_1{}^{fus}}{T_{m,1}}} \tag{42}$$

The eutectic concentration is then given by

$$\frac{\frac{2v_F^S\sigma_F^{SL}}{r} - \Delta H_F^{fus}}{R\ln[(1-x_E)\gamma_F^L] - \frac{\Delta H_F^{fus}}{T_{m,F}}} = \frac{\frac{2v_P^S\sigma_P^{SL}}{r} - \Delta H_P^{fus}}{R\ln(x_E\gamma_P^L) - \frac{\Delta H_P^{fus}}{T_{m,P}}} \tag{43}$$

2.3.2. Freezing and precipitation liquidus line and eutectic point calculation for the water/glycerol system.

After finding the general form of the conditions for solid–liquid equilibrium, the next step is to solve this set of equations for the system of interest in this chapter, which is the water/glycerol system. We want to compute the liquidus lines of the phase diagram, *i.e.,* the freezing point as a function of composition (solidification of solvent water) and the precipitation saturation composition as a function of temperature (solidification of solute glycerol). We wish to compare such a phase diagram computed in the presence of a curved solid–liquid interface (*i.e*., confined in a capillary) to the traditional phase diagram computed for a flat solid–liquid interface (unconfined).

Figure 4 shows a schematic diagram of the system with curved solid–liquid interfaces and contact angles of zero. The left figure refers to the freezing process and the right figure refers to the precipitating process. Component 1 represents the molecules that are present in both solid and liquid. Therefore, in the freezing process component 1 is water and component 2 is glycerol.

For the precipitating process, component 1 represents glycerol and component 2 represents water. According to the Gibbs Surface of Tension approach[5] we have adopted, the solid–liquid interfacial tension is independent of curvature.

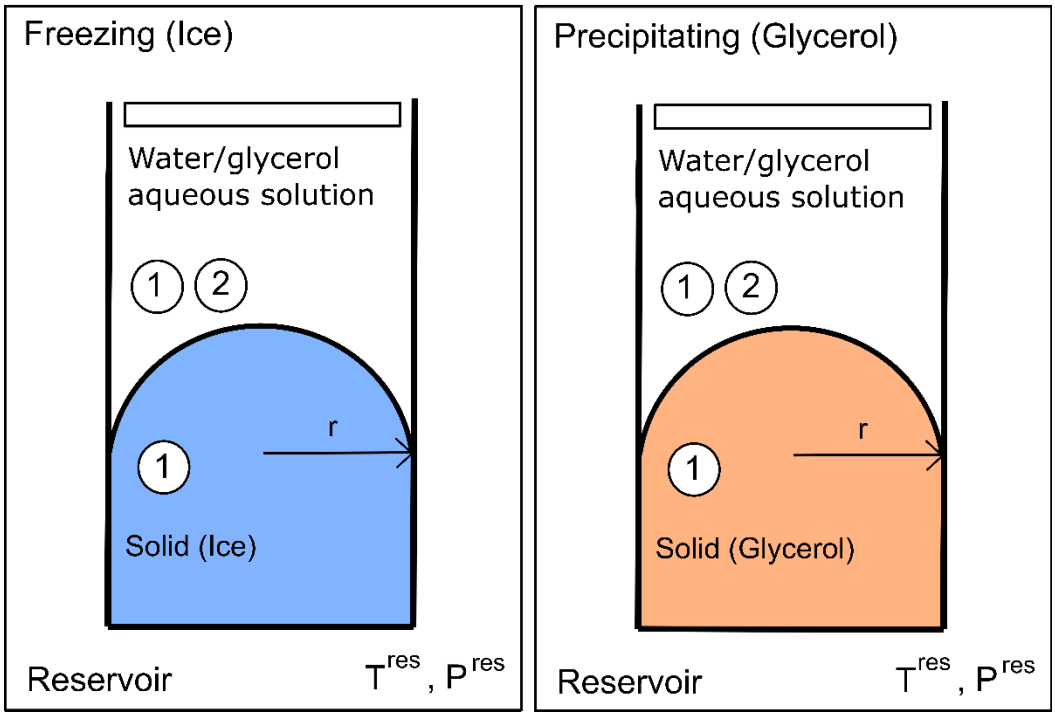

Figure 4. Schematic diagram of equilibrium with a curved solid–liquid interface and contact angle of zero. The freezing process is shown in the left panel and the precipitating process is shown in the right panel.

For all of the preceding equations we have used the index 1 for the component that exists in both solid and liquid phases. Thus, for the left liquidus line (freezing of water as the solid), component 1 refers to water molecules, and all the properties of water must be inserted into Equations (41) or (42). For the right liquidus line (precipitating of glycerol as the solid), component 1 represents glycerol molecules, and all the properties of glycerol must be inserted into Equations (41) or (42). The properties of pure water and pure glycerol are tabulated in Table 1.

Table 1. Properties of pure water and pure glycerol[46] at $P^L = 1$ atm

	$T_{m,1}$(K)	ΔH_1^{fus}(J/mol) at $T_{m,1}$	v_1^S(m^3/mol) at $T_{m,1}$
Water	273.15	6010	1.963×10^{-5}
Glycerol	291.35	18300	6.896×10^{-5}

2.3.3. Activity coefficient model

Equation (41) must be used along with a model to express the activity coefficient of component 1 (γ_1^L in Equation (41)). In this thesis, we consider a solution consisting of water and glycerol. To model the activity coefficients, we used the Margules model, and obtained the coefficients by fitting the model to solid–liquid equilibrium data for the water/glycerol system. For the water/glycerol system, the two-parameter Margules model gives a better fit compared to the osmotic virial equation.[47] γ_1^L is the activity coefficient of component 1, the component that is in both solid and liquid. To show the activity coefficients of different molecules clearly, here we use γ_w^L and γ_g^L to represent the activity coefficients of water and glycerol respectively. x_w^L is the mole fraction of water in the liquid, and x_g^L is the mole fraction of glycerol. According to the general Margules equation, the activity coefficients of the two components of a binary system are given by:

$$ln(\gamma_w^L) = b_w(x_g^L)^2 + c_w(x_g^L)^3 + \cdots \quad (44)$$

$$ln(\gamma_g^L) = b_g(x_w^L)^2 + c_g(x_w^L)^3 + \cdots \quad (45)$$

where coefficients b_g, c_g, ... are not independent, and are related to b_w, c_w, ... through the Gibbs–Duhem equation at constant temperature and pressure. γ_1^L should be replaced by γ_w^L from Equation (44) for the freezing process, and γ_1^L should be replaced by γ_g^L from Equation (45) for the precipitating process. Considering the dependency of the coefficients (through the Gibbs–Duhem equation), and truncating the polynomials to third-order terms, results in the two-parameter Margules equation:[48]

$$\ln(\gamma_w^L) = [A_{wg} + 2(A_{gw} - A_{wg})x_w^L](x_g^L)^2 \quad (46)$$

$$\ln(\gamma_g^L) = [A_{gw} + 2(A_{wg} - A_{gw})x_g^L](x_w^L)^2 \quad (47)$$

Parameters A_{wg} and A_{gw} are obtained by fitting Equation (41) in the absence of curvature ($r \to \infty$) , along with Equation (46) for the freezing process, or along with Equation (47) for the precipitating process, to the experimental data of temperature versus mole fraction of the left and right liquidus by minimizing the residual sum of squared errors. The Margules coefficients A_{wg} and A_{gw} are considered to be independent of temperature.

2.4. Results and Discussion

2.4.1. Margules coefficients for the water/glycerol system from experimental data[49]

This part was done by Leila Zargarzadeh, and is not shown here as the content of the thesis. The full content is included in published reference.[78] The resulting Margules parameters A_{wg} and A_{gw} are given in Table 2 and were used for calculations in the following sections.

Table 2. Parameters obtained from fitting the two-parameter Margules model to the experiment data of Lane[49] at P^L =1 atm.

A_{wg}	A_{gw}
-1.0952	-2.1641

2.4.2. Effect of curvature on the solid–liquid equilibrium phase diagram and the eutectic point for the water/glycerol system

Equation (41) gives the relationship between equilibrium temperature (T) and liquid mole fraction of the solidifying component (x_1^L). Values for the parameters $T_{m,1}$, ΔH_1^{fus}, and v_1^S can be found in Table 1. The activity coefficients of component 1 can be calculated from Equations (46) or (47) with the parameters of the two-parameter Margules model shown in Table 2.

The interfacial tension is dependent on temperature and concentration,[50] but it is hard to measure the interfacial tension of a nanoscale solid particle with liquid directly by experiment.[51] It should be noted that the main goal of this article is to investigate the effect of curvature on the freezing and precipitating liquidus lines and on the eutectic point. Knowing the exact value of the interfacial tension would allow quantitative prediction of the equilibrium temperatures for the freezing and precipitating processes; however the value is subject to change with the system's conditions. For simplicity, we assumed that the interfacial tension is constant and independent of temperature and concentration. We investigate the curvature effect at constant capillary radius r using 32 mN/m[52] as the interfacial tension of the ice–aqueous solution interfacial tension. There is a lack of experimental data and theoretical models for interfacial tension of glycerol precipitate with glycerol aqueous solution. Therefore, we make computations over a range of

possible solid glycerol–aqueous solution interfacial tensions (100 mN/m, 32 mN/m, 10 mN/m, 1 mN/m). Figure 5 shows the temperature of equilibrium as a function of concentration where the radius of the capillary changes from 1 μm to 100 nm, 10 nm, and 5 nm for various possible values of interfacial tension.

According to Figure 5(a) and (b) when the radius of the capillary is 1 μm or 100 nm, the freezing point and the solubility limit are not appreciably different from those of the flat surface. When the radius of the capillary decreases down to 10 nm, as shown in Figure 6(c), the freezing point is significantly decreased and the decrease becomes larger when the capillary radius is reduced further down to 5 nm as shown in Figure 5(d).

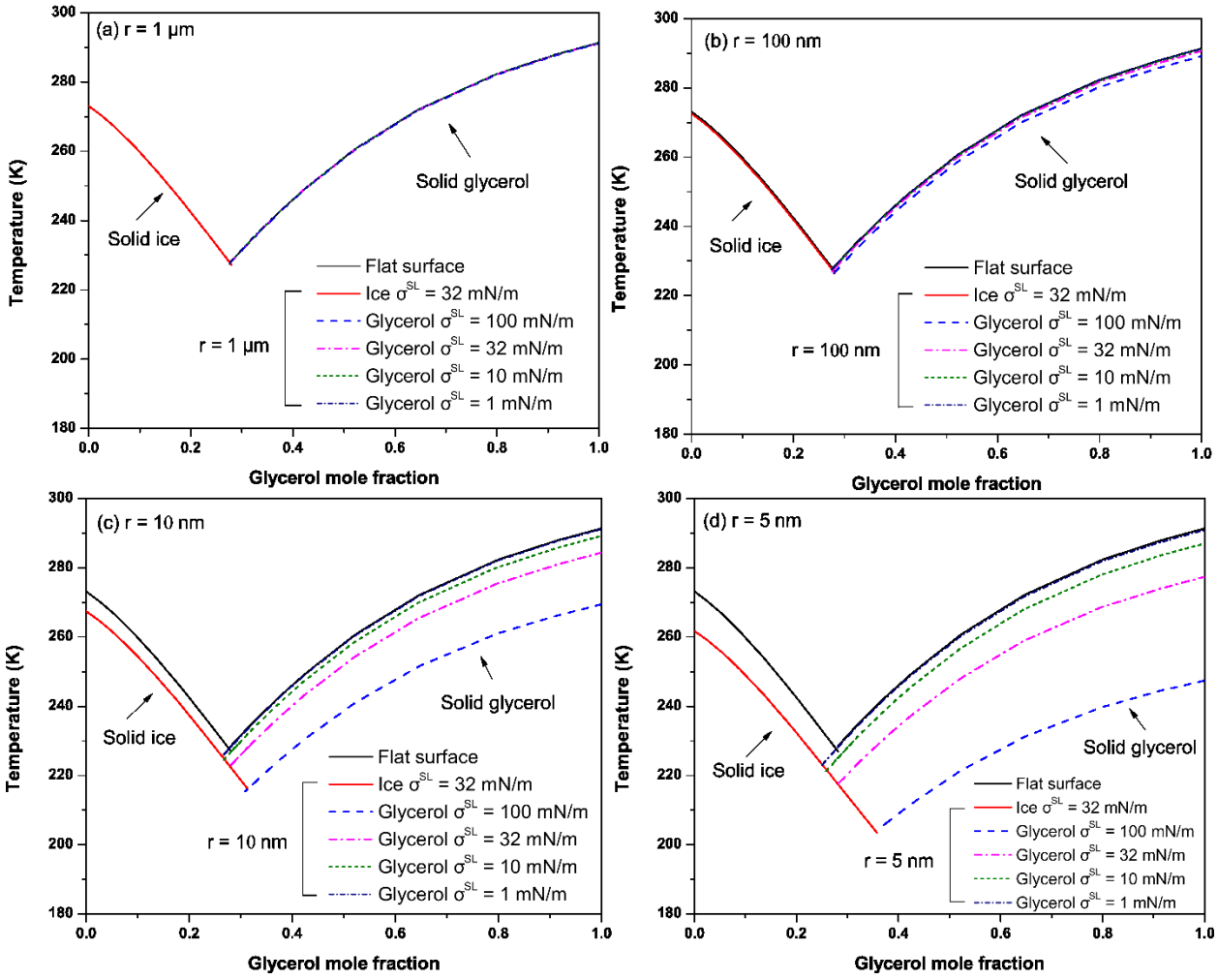

Figure 5. Predicted solid–liquid equilibrium phase diagram for the binary system of water and glycerol in capillaries at $P^L = 1$ atm with radii of (a) 1 μm, (b) 100 nm, (c)10 nm and (d) 5 nm. Predictions are done over a range of possible glycerol solid–liquid interfacial tension values for lack of data to do precise calculation.

The freezing point line (left hand liquidus) and the precipitating line (right hand liquidus) meet at the eutectic point. The eutectic point can be found by solving Equation (43) together with Equation (41) to see how the eutectic point temperature and concentration change with curvature. Figure 6 and Figure 7 predict the eutectic point temperature and concentration as a function of radius of curvature in the range from 5 nm to 100 nm. Figure 6 shows how the eutectic point temperature changes with radius of curvature. The eutectic point temperature of the

water/glycerol system decreases as the radius of the capillary decreases. When the radius of curvature is around hundreds of nanometers, the eutectic point does not change appreciably as a function of the curvature. When the radius of curvature is under 100 nm, the eutectic point temperature has a significant drop from its flat interface value.

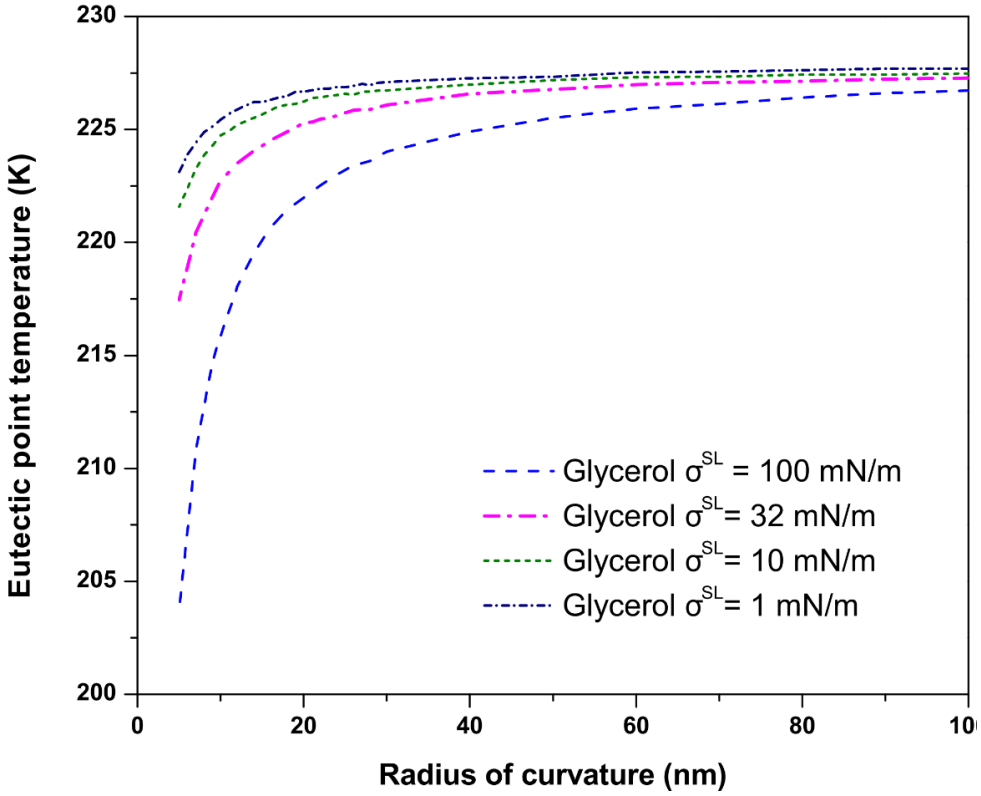

Figure 6. Predicted eutectic point temperature as a function of radius of curvature at $P^L = 1$ atm. Predictions are done over a range of possible glycerol solid–liquid interfacial tensions for lack of data to do a precise calculation.

Figure 7 shows that the eutectic point concentration changes as a function of radius of curvature. The eutectic point concentration stays almost the same when the radius of curvature is above 100 nm. When the radius of curvature is less than 100 nm, the trend of eutectic point concentration change depends on the difference between solid glycerol–liquid interfacial tension

and solid ice–liquid interfacial tension. If the glycerol σ^{SL} is bigger than the ice σ^{SL}, then the precipitating liquidus changes more than the freezing liquidus, which makes the eutectic point concentration increase as the radius of curvature decreases. If the glycerol σ^{SL} is smaller than the ice σ^{SL}, then the freezing liquidus changes more than the precipitating liquidus, which makes the eutectic point concentration decrease as the radius of curvature decreases. Regardless of the trend, the eutectic concentration changes significantly when the radius of curvature becomes less than 100 nm.

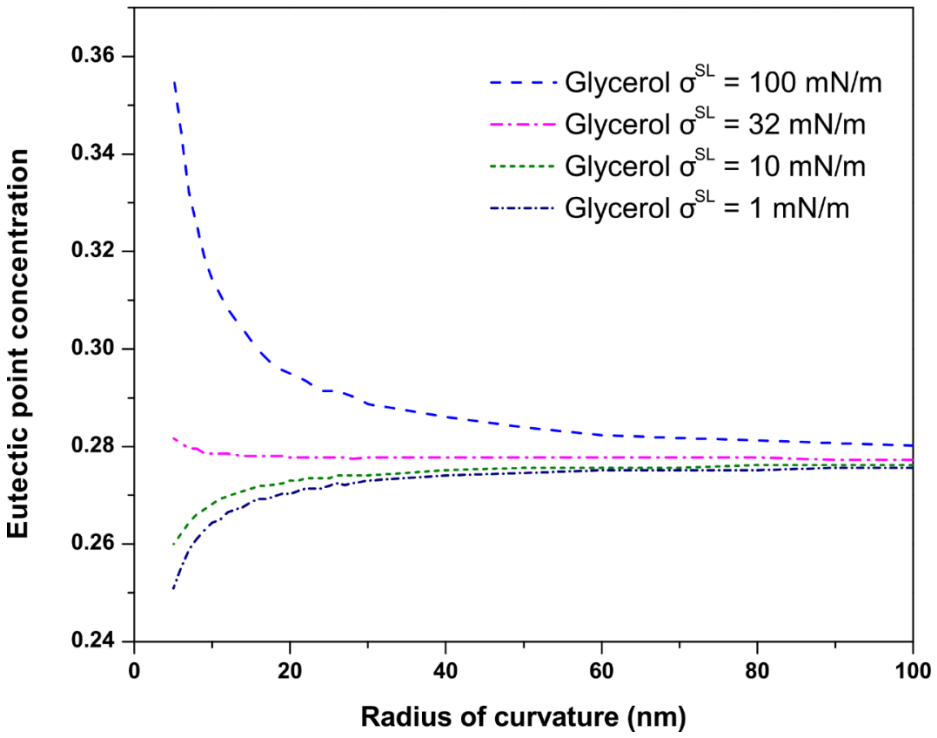

Figure 7. Predicted eutectic point concentration as a function of radius of curvature at $P^L = 1$ atm. Predictions are done over a range of possible glycerol solid–liquid interfacial tensions for lack of data to do a precise calculation.

2.5. Conclusion

We have presented a derivation of thermal, mechanical and chemical equilibrium conditions for solid–liquid equilibrium in a capillary of radius r, with different contact angles. We investigated the effect of curvature on solid–liquid equilibrium for the water/glycerol system. Curvature affects both the freezing process and the precipitating process. The solidifying points and the eutectic point temperature decrease as the radius of the capillary decreases and when the radius of curvature is reduced to the nanoscale, the decrease becomes significant. The derived conditions for equilibrium shown for solid–liquid equilibrium can be applied to other multicomponent systems in capillary pores. The calculation procedure presented for a multicomponent phase diagram with curvature provides a way of combining chemical potential equilibrium with the mechanical equilibrium of a curved solid–liquid interface.

There are limitations to this work that can be enumerated and discussed: (1) The Margules parameters are considered to be independent of temperature. (2) The interfacial tensions between each solid and the aqueous liquid solution were taken to be constants, independent of curvature, concentration and temperature. The shift of freezing point and eutectic point could be made accurately using the methods presented in this work if the glycerol solid–liquid interfacial tension were known. (3) Our calculations are based on the assumption that both ice–liquid and glycerol precipitate–liquid interfaces make a zero contact angle with the capillary solid wall.

This study gives a promising theoretical method to predict thermodynamic properties of solid–liquid equilibrium across a curved interface in nonideal multicomponent systems (demonstrated here for a binary system but extendable to multicomponent cases) that has applications in many fields such as cryobiology, forestry, and soil sciences. In cryobiology, the

freezing point of solutions containing diverse solutes, including salts, cryoprotectants, proteins, and many other macromolecules in confined spaces such as membrane pores is of vital importance.[19,20,21,42,45] Furthermore, during freezing, direct cell injury has been associated with eutectic crystallization.[53] In forestry, in the xylem parenchyma of hardwood tree species and in dormant flower bud primordia of woody species, extracellular water exists in microcapillaries in the extracellular space.[19] These microcapillaries can depress the freezing point of water in the intercellular spaces, and impede the spread of ice through the tissue. The freezing point depression of the microcapillaries can help the plant survive at low temperature. In soil science, the freezing and melting of water in porous particles that are abundant in soil are of critical interest in cold regions because of their role in frost damage. Previously, the solid–liquid equilibrium inside porous media has been studied for ice with pure water.[54,55] With our equations, the prediction of freezing and melting temperatures in nanoscale pores in soil could be extended to water that contains various soluble substances, such as salt or organic components that are abundant in soil.

3. Freezing of aqueous electrolytes in zinc–air batteries: Effect of composition and nanoscale confinement

3.1. Abstract

Zinc–air batteries, which typically employ aqueous electrolytes, have attracted much attention owing to high energy density, low cost and environmental friendliness. While the zinc–air battery is a promising solution for energy grid applications, the freezing of the electrolyte is an important problem for operation in cold climates. The freezing point of the electrolyte can be affected not only by chemical composition, but also by micro/nanoscale confinement in porous electrodes or separators. In this work, we first find osmotic virial coefficients by fitting experimental freezing point data for various electrolytes that are used in zinc–air batteries. Secondly, we show how additives that improve the performance of the batteries may also lower the freezing point of the electrolyte system. Thirdly, we show how the nanoscale confinement inside zinc–air batteries further decreases the freezing point; a 10 nm diameter capillary pore can suppress the local freezing point of the electrolyte by ~10 °C. Finally, we map out the equilibrium mol% ice as a function of temperature, concentration, and confinement. This study can provide insight to design tailored electrolytes specialized for low temperature applications.

3.2. Introduction

3.2.1. Zinc–air battery configuration

Large scale secondary rechargeable batteries, which store electricity in reversible chemical energy format, are the key component for energy grid storage, where electrical energy is stored during times when electricity generation exceeds consumption. In remote communities where electricity supply is off-grid (*i.e.*, no electric cable connection from a major power plant), including those in northern Canada, such large scale energy storage is especially needed because the supplies for electricity generation (such as diesel or hydro power) may be intermittent or even inconsistent.[56] In cold environments, freezing of the electrolyte is a critical issue.

While lithium-ion batteries dominate the rechargeable energy storage market, metal–air secondary batteries are expanding owing to their high specific energy, low material cost, and environmental friendliness.[57] Several metals have been proposed for metal–air batteries, such as lithium, magnesium, aluminum, iron and zinc.[58] Lithium–air batteries have the highest specific energy (5928 W h kg^{-1}) and high cell voltage (2.96 V) and are shown to have 5 to 10 times more energy density than standard lithium-ion batteries, but the current lithium–air battery is unstable when exposed to moist air or aqueous electrolyte.[59] Lithium salt and alkaline aqueous solution can be used in an aqueous electrolytic type of lithium–air batteries.[57,60,61] Magnesium and aluminum are also good candidates in terms of high energy density and relative stability with aqueous electrolyte, but they are low in reduction potential which leads to poor coulombic charging efficiency.[57] Electrolytes that can be used in magnesium–air batteries are NaCl, $KHCO_3$, NH_4NO_3, $NaNO_3$, or a solution of $NaNO_3$ and HNO_3, $NaNO_2$, Na_2SO_4, $MgCl_2$, $MgBr_2$, and $Mg(ClO_4)_2$.[62] For aluminum–air batteries, the choice of electrolyte can be flexible; the

electrolyte can be salt (such as sodium chloride), sea water, or alkaline electrolytes (such as potassium hydroxide).[63] However, the aluminum–air battery is not rechargeable; the battery stops working when the aluminum anode is consumed by the reaction of oxygen forming hydrated aluminum oxide.[64]

Zinc, which is abundant in the Earth's crust, has a good balance between specific energy (1084 W h kg^{-1}), cell voltage (1.65 V) and cost, and is considered to be the most economically feasible battery material for grid energy storage.[59,65,66] Alkali hydroxides (NaOH, LiOH, and KOH) are among the commonly used zinc–air battery electrolytes. KOH (potassium hydroxide) is the most frequent choice due to having the highest ionic conductivity with K^+, the lowest viscosity for mass transport, fast electrochemical kinetics, and high solubility of zinc salts.[67] The concentration range of KOH is between 20 and 45 wt% KOH in the aqueous solution; ~30 wt% KOH provides the maximum ionic conductivity (around 640 mS cm^{-1}).[68,69] For low temperature applications (down to −30 °C), a slightly higher concentration (30–40% KOH) is preferred.[67] The electrolyte is of vital importance in the battery performance in many aspects such as capacity retention and cycling efficiency. Aqueous alkaline electrolytes, which are commonly used in metal–air batteries, have strong advantages including excellent conductivity, high reaction kinetics with oxygen, and a wide choice of electrocatalyst materials.

In this study, we focus on the thermodynamic properties of the electrolyte system in zinc–air batteries at low temperature. As shown in Figure 8, zinc–air batteries are composed of four components: a zinc electrode which works as the anode, a cathode comprising a catalyst-painted gas diffusion layer (GDL), a separator and an alkaline electrolyte.[66] The separator is in between the two electrodes, and acts as a physical barrier that prevents physical contact of the two electrodes which would cause a short-circuit. The role of the separator is to allow the transport of

hydroxyl ions from the air electrode to the zinc electrode. Therefore, stability in alkaline solution, high ionic conductivity and appropriate pore size are required.[67,70]

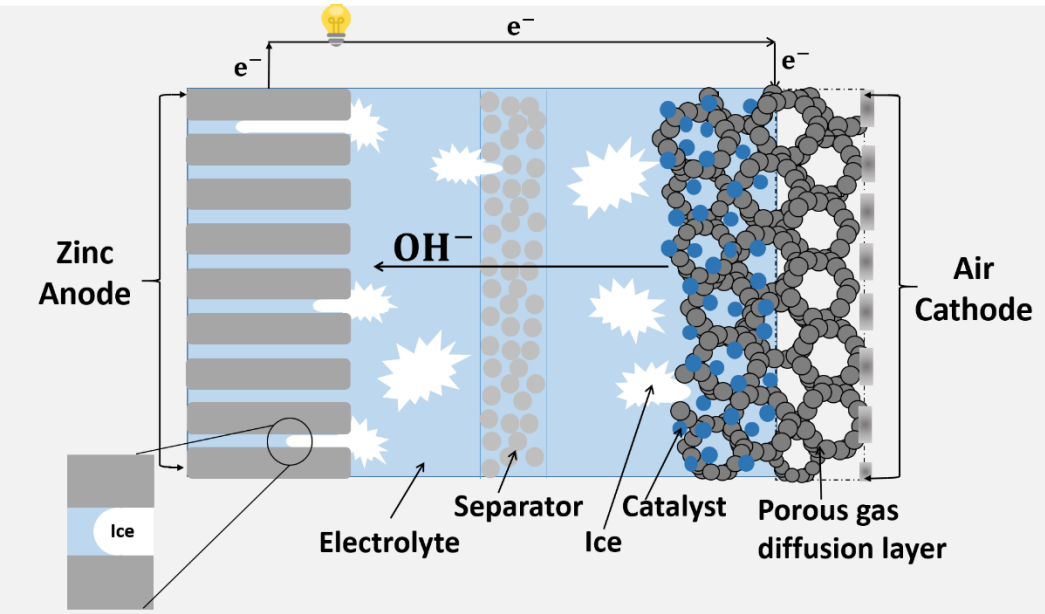

Figure 8. Schematic of zinc–air battery configuration and ice formation at low temperature.

Based on the reaction equations mentioned below, zinc–air batteries need an open structure to react with oxygen. The zinc electrode works as an anode. There are two reaction steps on the zinc electrode; the first step is:

$$Zn + 4OH^- \Leftrightarrow Zn(OH)_4^{2-} + 2e^-, \tag{48}$$

and the second step is:

$$Zn(OH)_4^{2-} \Leftrightarrow ZnO + H_2O + 2OH^-. \tag{49}$$

The reaction on the air cathode is:

$$O_2 + 2H_2O + 4e^- \Leftrightarrow 4OH^-. \tag{50}$$

Thus, the overall reaction is:

$$2\mathrm{Zn} + \mathrm{O}_2 \Leftrightarrow 2\mathrm{ZnO}. \tag{51}$$

Zinc–air batteries still have several unsolved drawbacks. For example, there are four major phenomena that can lower the performance of the zinc electrode: dendrite growth, shape change, passivation induced internal resistance, and hydrogen evolution. Firstly, zinc dendrites, sharp, needle-like metallic protrusions that cause a short-circuit between the cathode and anode, are electrochemically grown during battery operation.[21,71–74] Secondly, the shape of the zinc electrode changes due to build-up of internal stresses. Thirdly, passivation of the zinc electrode by ZnO precipitation causes an increase of internal resistance. Fourthly, the hydrogen evolution reaction consumes some of the electrons provided during charging, resulting in less than 100% coulombic efficiency at the zinc electrode. Currently, blending additives into the electrolyte is an essential method to reduce the adverse effects from these drawbacks.[75] For example, additives can adsorb onto active hydrogen evolution sites, resulting in a reduced solubility of $\mathrm{Zn(OH)}_4^{2-}$ that leads to early ZnO precipitation.[76] This method can improve the performance of the zinc electrode by increasing the efficiency of the anode reaction.

Introducing nanoscale pores is also an important strategy in enhancing zinc–air battery performance. The performance of zinc electrodes is heavily dependent on their porous morphology that increases the surface area while maintaining efficient ionic transport.[66] The nanoporous zinc structure presents a modified activation energy for electrochemical cycling. For example, the hierarchical nanoporous structure of the zinc electrode allows high surface area and efficient ion diffusion of zinc in alkaline mediums.[77] In addition, the performance of the air cathode depends on the effective functioning of the air electrode porosity for air permeation. At

low temperatures, ice formation in these pores results in serious damage to the structure. So understanding the effect of the nanoporous structure on freezing of the electrolyte system of zinc–air batteries is of vital importance.

The additives we choose in this study can be added to aqueous electrolytes to improve the performance of zinc–air batteries. Nanoporous structure can be found in the separator, zinc anode and air cathode; confinement of electrolyte can be found in these three places. At low temperature as shown in Figure 8, the nanoporous structure in the separator, zinc anode electrode, and air cathode electrode can alter the freezing behavior due to confinement of the aqueous electrolyte.[70] When the temperature decreases, ice can form in the electrolyte, but a lower temperature is required for ice to form or propagate inside the pores of the separator or two electrodes than in the unconfined electrolyte. Here, we focus on investigating the thermodynamic properties that describe freezing behavior of the aqueous electrolyte with additives, both in bulk and in nanoscale confinement by pores in zinc–air batteries.

3.2.2. Freezing point depression of electrolyte aqueous solutions with the multisolute osmotic virial equation

To our knowledge, investigation of the freezing point of relevant electrolyte systems over a range of concentration with the effect of nanoscale confinement has not been done before.

The freezing point depression of an aqueous solution confined in a pore can be expressed[78] (Chapter 2; Equation (37)) as a function of concentration and pore radius r

$$T_{m,1} - T = \frac{2v_1^S \sigma^{SL} T_{m,1} \cos\theta}{r\Delta H_1^{fus}\left(1 + \frac{RT_{m,1}\tilde{\pi}}{\Delta H_1^{fus}}\right)} + \frac{R\tilde{\pi}T_{m,1}^2/\Delta H_1^{fus}}{1 + R\tilde{\pi}T_{m,1}/\Delta H_1^{fus}} \quad (52)$$

where $T_{m,1}$ is the melting point of pure water at the pressure of the bulk phase (*i.e.*, liquid phase pressure P^L), T is the freezing point of the aqueous solution, v_1^S is the molar volume of pure water in solid phase at $T_{m,1}$ and P^L, R is the universal gas constant, σ^{SL} is the ice–solution interfacial tension, ΔH_1^{fus} is the molar enthalpy of fusion (latent heat of melting) for pure water at $T_{m,1}$ and P^L, θ is the contact angle between the ice–solution interface and the pore wall, and $\tilde{\pi}$ is the osmole fraction of the solution, (a function that describes solution thermodynamic nonideality). Equation (52) is a nonideal form of the Gibbs–Thomson equation. The properties of pure water at $P^L = 1$ atm are shown in Table 3.

Table 3. Properties of pure water at $P^L = 1$ atm.[79]

	$\boldsymbol{R}$(J/(mol K))	$\boldsymbol{T_{m,1}}$(K)	$\boldsymbol{\Delta H_1^{fus}}$(J/mol) at $\boldsymbol{T_{m,1}}$	$\boldsymbol{v_1^S}$(m^3/mol) at $\boldsymbol{T_{m,1}}$
Water	8.314	273.15	6010	1.963×10^{-5}

What remains is to describe the nonideality of the aqueous solution with the osmole fraction as a function of the mole fractions of solutes. The osmotic virial equation is an accurate, straightforward, predictive method used to represent osmole fraction as a polynomial in mole fraction.[42] The single-solute osmotic virial equation for solute i in the electrolyte is: [42,80]

$$\tilde{\pi} = k_i^* x_i + B_{ii}^*(k_i^* x_i)^2 + C_{iii}^*(k_i^* x_i)^3 + \cdots \quad (53)$$

where x_i is the mole fraction of solute i, and B_{ii}^* and C_{iii}^* are the second and third mole-fraction-based osmotic virial coefficients of solute i (unitless), respectively. The second osmotic virial coefficient represents the interactions between two solute i molecules; the third osmotic virial coefficient represents interactions between three solute i molecules, *etc*. These coefficients are

zero if solute i is thermodynamically ideal. For electrolyte solutes, solute concentration must be multiplied by an additional parameter, the mole-fraction-based dissociation constant of solute i, k_i^*. This dissociation constant accounts empirically for ionic dissociation and other electrolyte effects.[80] The osmotic virial coefficients and the dissociation constants may be obtained by fitting the single-solute osmotic virial equation to single-solute solution data, with each solute having unique coefficients.

The solution nonideality of multisolute solutions can be predicted from tabulated single-solute properties using the Elliott *et al* form of osmotic virial equation:[42,81,82]

$$\tilde{\pi} = \sum_{i=2}^{z} k_i^* x_i + \sum_{i=2}^{z}\sum_{j=2}^{z}\left[\frac{\left(B_{ii}^* + B_{jj}^*\right)}{2} k_i^* x_i k_j^* x_j\right] + \sum_{i=2}^{z}\sum_{j=2}^{z}\sum_{k=2}^{z}\left[\left(C_{iii}^* C_{jjj}^* C_{kkk}^*\right)^{1/3} k_i^* x_i k_j^* x_j k_k^* x_k\right] + \cdots \quad (54)$$

where $i, j, k = 2$ to z represent the $z - 1$ solutes in the solution.

3.2.3. Objectives of this work

In this chapter, we investigate the freezing behavior of single-solute and multisolute electrolyte systems in zinc–air batteries including the effects of nanoscale confinement. We start by obtaining osmotic virial coefficients and dissociation constants of relevant electrolytes by fitting single-solute freezing point data with the osmotic virial equation. Then, we plot freezing temperature as a function of concentration for unconfined and confined electrolyte systems. The effects of different pore radii and different amounts of additives are investigated. In order to conceptualize a quantitative picture of partially frozen electrolytes at equilibrium to benefit

battery designers, the mol% ice formed at a given temperature for specific electrolyte systems is calculated. This work provides theoretical predictions of the additive effect and ice–solution curvature effect on the freezing behavior of electrolyte systems in zinc–air batteries at low temperature, and can be extended to other low temperature secondary batteries containing different solutions.

3.3. Osmotic virial coefficients for electrolytes of interest

First we fit the osmotic virial equation to the freezing point data of unconfined single-solute electrolyte solutions and get the single-solute osmotic virial coefficients and dissociation constants. For unconfined electrolyte solutions where $r \to \infty$, Equation (52) can be expressed as:

$$T_{m,1} - T = \frac{R\tilde{\pi}T_{m,1}^2}{\Delta H_1^{fus} + R\tilde{\pi}T_{m,1}} \tag{55}$$

Equation (55) can be rearranged to:

$$\tilde{\pi} = \frac{(T_{m,1} - T)\Delta H_1^{fus}}{RT_{m,1}T} \tag{56}$$

Equation (56) is used to convert experimentally measured freezing points to osmole fractions for single-solute solutions. This data as a function of mole fraction can be fit to Equation (53) to yield values for the single-solute osmotic virial coefficients.

To determine the number of parameters to include in the fit (*i.e.*, the order of the osmotic virial polynomial and whether or not to include a dissociation constant), in each case, we start with no parameters and progressively increase the number of parameters until the adjusted R^2 increase becomes less than 0.005 upon addition of a new parameter (p equals 1 or 2 for the cases considered here). A regression-through-the-origin (RTO) form of adjusted R^2 was used:[42]

$$R^2_{adj.RTO} = 1 - \frac{\sum\left(y_{(a)} - \hat{y}_{(a)}\right)^2/(n-p)}{\sum\left(y_{(a)}\right)^2/(n)} \quad (57)$$

where $y_{(a)}$ is the value of the a^{th} data point, $\hat{y}_{(a)}$ is the fitted model prediction of the a^{th}data point, n is the total number of data points, and p is the number of parameters/coefficients in the model.

An example of the fitting is shown in Figure 9 for KOH.

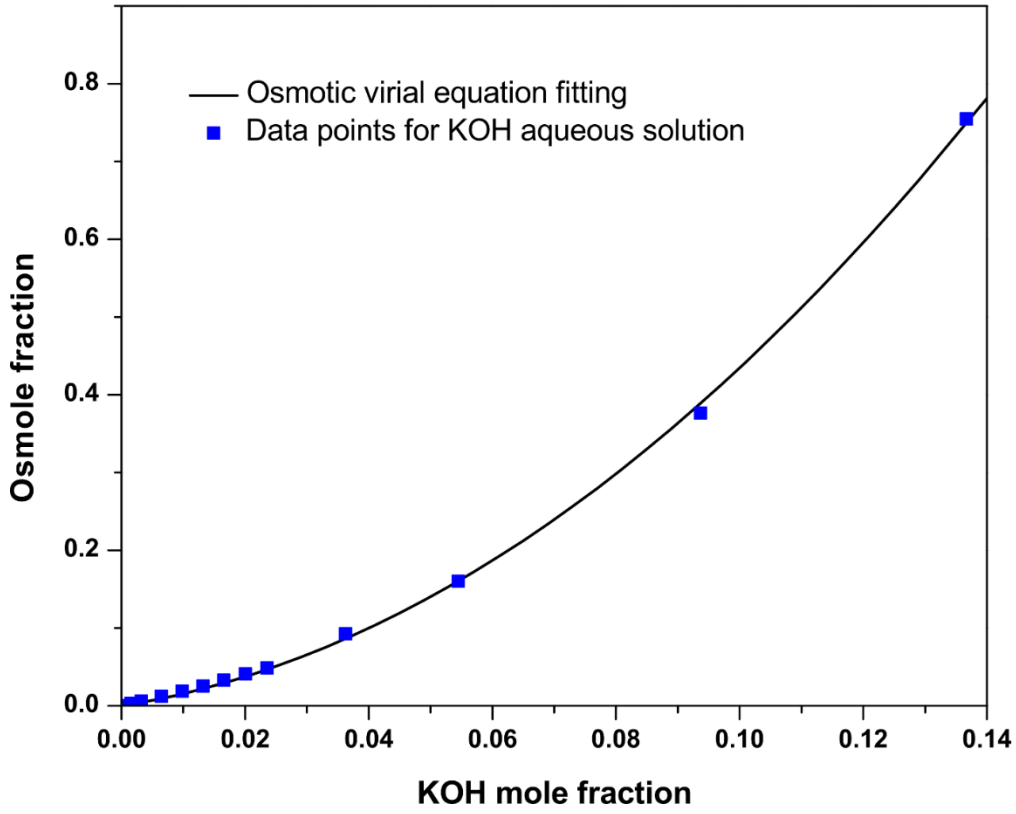

Figure 9. Best fit of the mole-fraction-based osmotic virial equation to experimental data for the freezing of unconfined aqueous KOH solutions.[79,83] Equation (56) and the properties in Table 3 were used to convert the freezing point data from references[79] and [83] into osmole fraction as a function of mole fraction. The data was then fit to Equation (53) yielding k^*_{KOH} and B^*_{KOH}. Here the number of parameters, *p*, is 2.

The best fit parameters of the osmotic virial equation for different electrolytes commonly added to improve the performance of zinc–air batteries are shown in Table 4. For example,

K_2CO_3, K_2HPO_4, Na_2CO_3, Na_3PO_4, and Na_2HPO_4 are additives that can be added in the electrolyte to reduce zinc dissolution.[68,84–86] Citric acid and H_3PO_4 are proposed to prevent dendrite growth and increase hydrogen overpotential.[87,88] The maximum mole fraction of each data set is also given in Table 4. Care should be taken not to use the fit parameters in Table 4 above the maximum range of the data fit since the extrapolated polynomial may not describe freezing behavior, for example, beyond a eutectic point.

Table 4. Obtained osmotic virial coefficients B_{ii}^* and dissociation constants k_i^* along with 95% confidence intervals for different electrolyte additives. n is the number of data points and p is the number of parameters used in the osmotic virial equation. Adjusted R^2 of the fit and the maximum mole fraction of the data are also given.[79,83]

	n	p	$k_i^* \pm 95\%\ CI$	$B_{ii}^* \pm 95\%\ CI$	$R^2_{adj,RTO}$	Max. mole fraction	Molar mass (g/mol)
KOH	13	2	1.259 ± 0.191	19.48 ± 6.940	0.99955	0.1367	56.1056
K_2CO_3	21	2	1.369 ± 0.253	25.10 ± 11.36	0.99800	0.07989	138.205
K_2HPO_4	13	1	2.174 ± 0.023	0	0.99966	0.008905	174.2
Na_2CO_3	7	1	1.967 ± 0.06	0	0.99867	0.01072	105.9888
Citric acid	21	1	1.088 ± 0.004	0	0.99992	0.03860	192.124
H_3PO_4	26	2	0.8948 ± 0.0304	16.01 ± 1.530	0.99987	0.1091	97.99
CH_3OH	28	2	0.8786 ± 0.0329	3.574 ± 0.396	0.99964	0.4573	32.04
Na_3PO_4	5	1	2.889 ± 0.197	0	0.99559	0.002807	163.94
Na_2HPO_4	3	1	2.364 ± 0.237	0	0.99837	0.001929	141.96

3.4. Predictions of the role of composition and confinement on the freezing point of electrolytes

Now that we have the required osmotic virial equation parameters, we can use them in Equation (52) to predict the freezing temperature of single-solute and multisolute electrolyte solutions as a function of pore radius and electrolyte composition and concentration. Here we wish to study the impact that curvature of the ice–solution interface makes on the freezing point. The porous geometry of electrodes in real zinc–air batteries may be complicated. We consider

confinement in an equivalent ice-wetting cylindrical pore, the contact angle, θ, between the ice–solution interface and the pore wall to be zero so that the pore radius gives the radius of curvature of the ice–solution interface. The results are relevant to real batteries so long as it is understood that the curvature of the ice–solution interface is determined by the contact angle that ice makes with the anode material and local dimensions between anode surfaces in a complicated geometry within which only an ice–solution interface with a specific curvature can be in equilibrium. There will be a range of relevant pore sizes. The lower the temperature, the smaller the pore in which ice can form or propagate as will be predicted in this work. For this work, we make the assumption that the interfacial tension between ice and unfrozen electrolyte solution is constant, *i.e.,* independent of temperature and concentration, and is equal to 32 $\mathrm{mJ/m^2}$.

Figure 10 shows the freezing point as a function of solute mole fraction predicted by Equation (52) for an unconfined aqueous KOH solution and aqueous KOH solutions confined in pores with a range of radii. When the pore radius is 1 μm or 100 nm, the freezing point of the KOH electrolyte is not appreciably different from that of the electrolyte without confinement. When the pore radius is reduced further down to 10 nm, the freezing point of the KOH electrolyte decreases significantly.

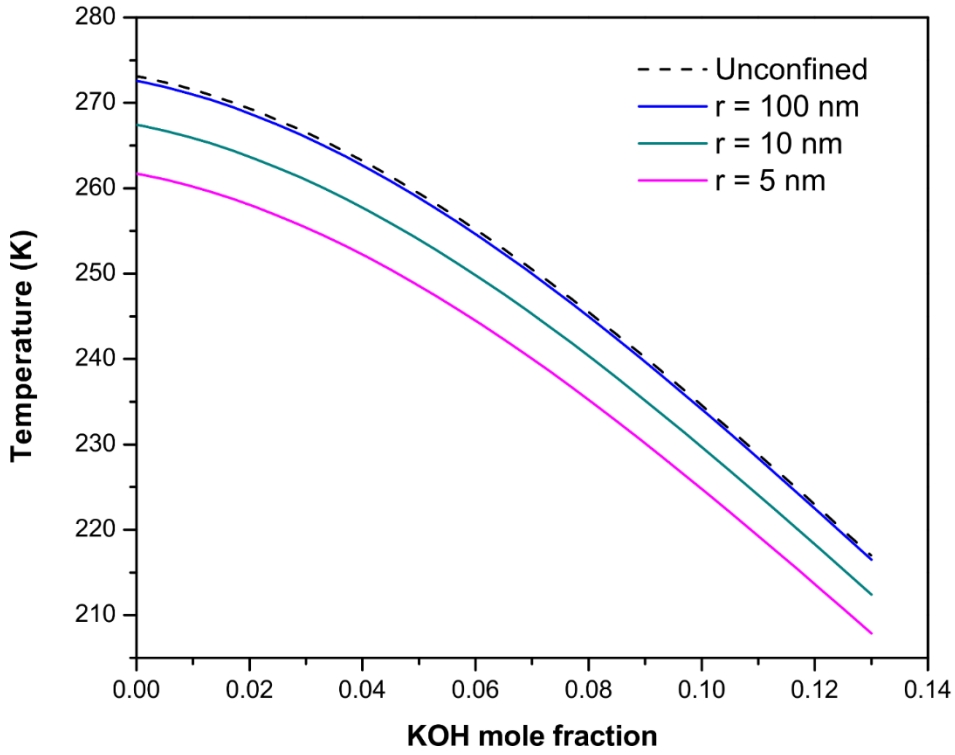

Figure 10. Predicted freezing point as a function of KOH mole fraction for an unconfined aqueous KOH solution and aqueous KOH solutions confined in pores with radii of 100 nm, 10 nm, and 5 nm. (Predictions for a pore with a radius of 1 μm directly underlie predictions for the unconfined electrolyte.) Calculations are made with Equation (52) with $\theta = 0$ and $\sigma^{SL} = 32$ mJ/m^2, and with the osmotic virial equation parameters given in Table 4.

To examine the freezing point of multisolute electrolyte solutions, we note that in the freezing process, pure water freezes to ice, and the ratio of the mole fractions of any two solutes in the remaining unfrozen solution will remain constant. We are interested in the effect of particular additives to the KOH solution so we consider two-solute systems and define the ratio $\boldsymbol{\eta}$ between mole fraction of additive $\boldsymbol{j}$ and mole fraction of KOH.

$$\eta = \frac{x_j}{x_{KOH}} \tag{58}$$

Substituting Equation (58) into Equation (54) for two solutes, and recognizing that for the solutes in Table 4 only terms up to second order are required, we get an equation for the osmole fraction of a solution with one additive and one main electrolyte solute.

$$\begin{aligned}\tilde{\pi} = k^*_{KOH}x_{KOH} + k^*_j x_j + B^*_{KOH}(k^*_{KOH}x_{KOH})^2 + B^*_{jj}\left(k^*_j x_j\right)^2 \\ + \left(B^*_{KOH} + B^*_{jj}\right)(k^*_{KOH}x_{KOH})\left(k^*_j x_j\right) \\ = (k^*_{KOH} + k^*_j\eta)x_{KOH} \\ +\left[B^*_{KOH}(k^*_{KOH})^2 + B^*_{jj}(k^*_j)^2\eta^2 + k^*_{KOH}k^*_j\left(B^*_{KOH} + B^*_{jj}\right)\eta\right](x_{KOH})^2\end{aligned} \quad (59)$$

Substituting Equation (59) into Equation (52), and using the parameters in Table 4, we can predict the freezing temperature of the electrolyte with additives as a function of concentration and confinement pore radius. Here, we use K_2CO_3 as an example of an additive (the second solute) to show the effect of different amount of additives on the freezing point in zinc–air batteries. Based on experimental relevance, we make computations over a range of mole fraction ratio η (between 0.1 and 1).[89–91]

Figure 11 shows the freezing point of electrolyte systems as a function of total solute mole fraction. Total solute mole fraction is the sum of the mole fraction of KOH and the mole fraction of additive. Figure 11 shows the pore size effect on the freezing point of the electrolyte system for K_2CO_3:KOH=1:1 (ratio $\eta = 1$).

.

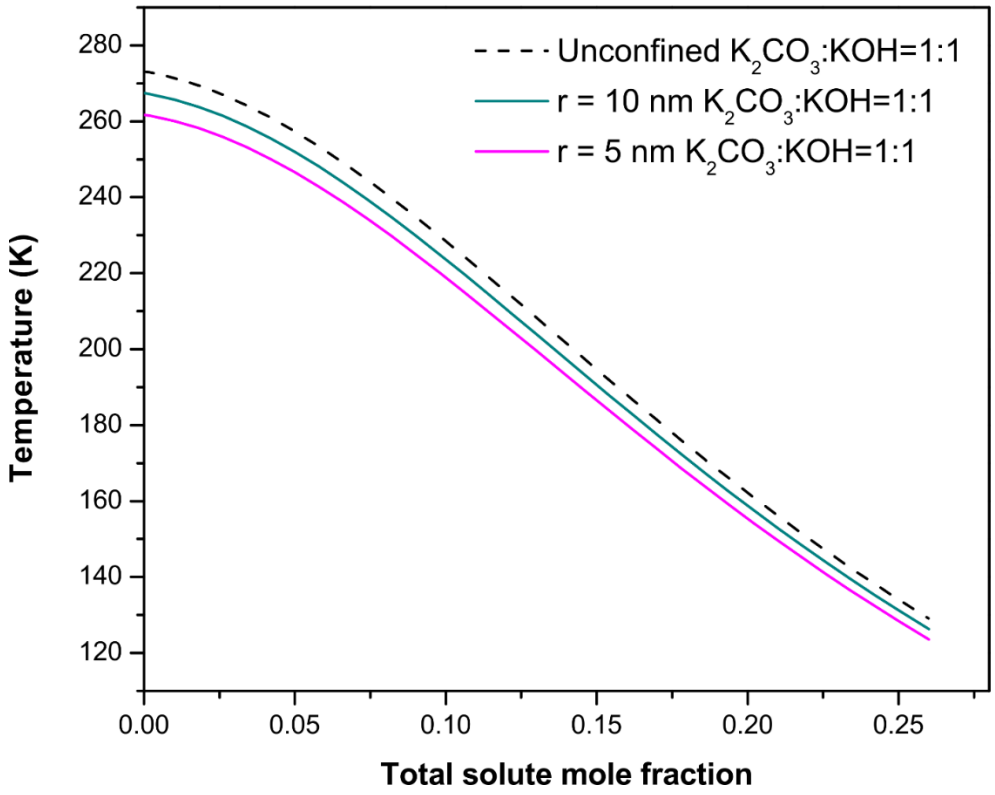

Figure 11. Predicted freezing point of KOH electrolyte with K_2CO_3 additive ($x_{K_2CO_3}: x_{KOH} = 1:1$) for unconfined electrolytes and for electrolytes confined in pores with radii of 10 nm, and 5 nm, assuming $\theta = 0$ and $\sigma^{SL} = 32$ mJ/m^2. (Note that predictions for 1 μm and 100 nm pores directly underlie the unconfined prediction.)

We then compare the effect of having different ratios between solute and additive by plotting the freezing point of electrolyte systems as a function of total solute mole fraction. Figure 12 shows the effect of the amount of K_2CO_3 additive on freezing point of the electrolyte system for an unconfined solution and within a 5 nm pore.

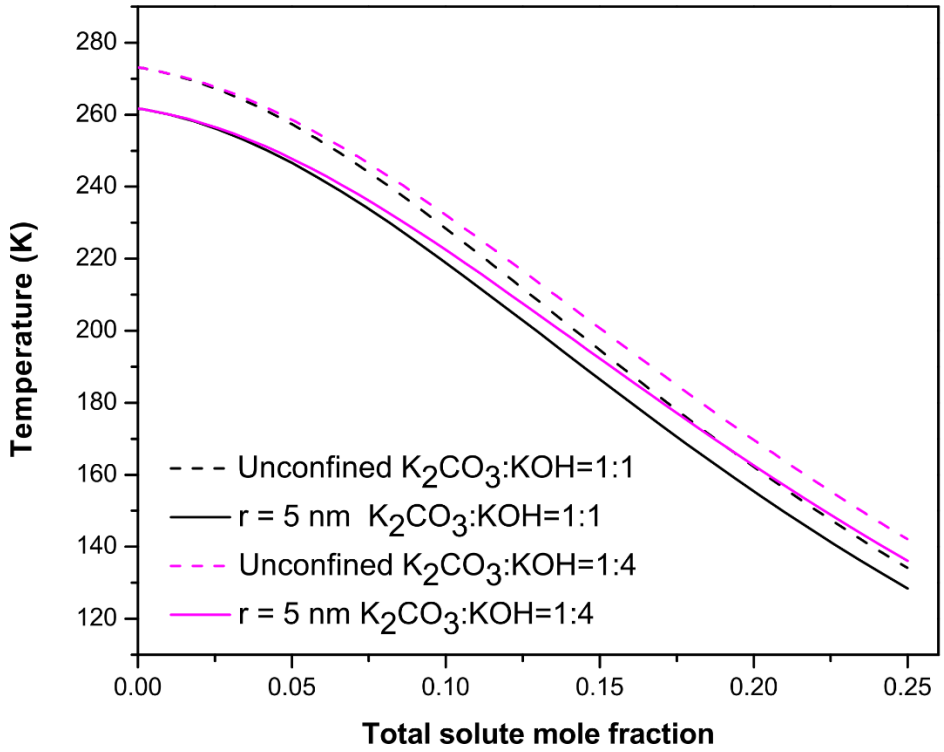

Figure 12. Predicted freezing point for electrolyte systems with different additives ratio K_2CO_3: KOH =1:1 or 1:4 ($\eta = 1, 0.25$) confined within a 5 nm pore, compared with unconfined electrolyte systems. Predictions assume $\theta = 0$ and $\sigma^{SL} = 32$ mJ/m^2. The predictions for KOH as the only solute (not shown) fall above the four lines.

Knowing the amount of ice at equilibrium in zinc–air batteries can shed light in estimating the performance of the batteries at low temperatures. Figure 13 shows schematically how the mol% of each phase can be determined from the predicted composition-dependent freezing point by the lever rule.[41] In Figure 13, x_i represents the initial total solute mole fraction before freezing, T_{given} represents the given temperature, and $x_{unfrozen\ solution}$ represents the mole fraction in the unfrozen solution at given temperature T_{given}.

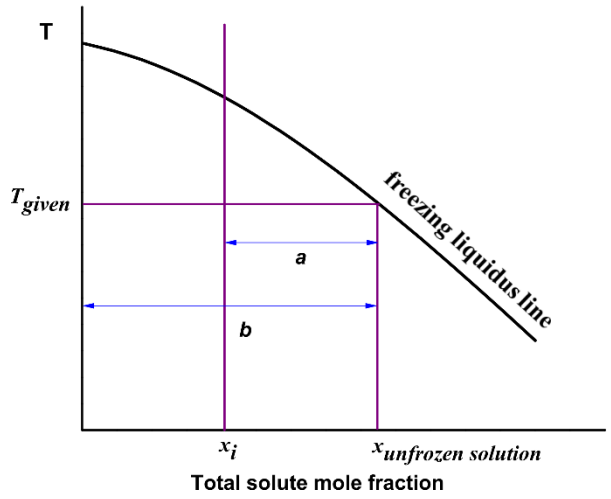

Figure 13. Schematic of binary phase diagram showing the lever rule.

Equation (60) can be used to calculate mol% ice at a given temperature for a given initial composition.

$$\text{mol\% ice} = \frac{N_{ice}}{N_{ice} + N_{water} + N_{solute} + N_{additive}} = \frac{a}{b} \tag{60}$$

$$= \frac{x_{unfrozen\ solution} - x_i}{x_{unfrozen\ solution}} \times 100\%$$

where N represents the number of moles, and a and b are the line segment lengths shown on Figure 13. Based on Equation (60), if the given initial mole fraction x_i increases, a decreases and b is constant for a fixed T_{given}, and mol% ice decreases. For a constant given initial mole fraction x_i, if the given temperature T_{given} decreases, $x_{unfrozen\ solution}$ increases, and mol% ice increases.

Figure 14 shows the mol% ice at a range of temperatures for four different electrolyte systems. Here, the combinations of two confinement conditions (unconfined *vs.* pore size r = 5 nm) and two solute concentrations (30 wt% KOH *vs.* 15 wt% KOH + 15 wt% K_2CO_3) are considered. The

curve shifts to the left (*i.e.*, less ice formation at a given condition) when the pore size decreases and when additives are added into the KOH electrolyte. In drawing Figure 14, predictions were stopped when either the temperature goes below the KOH eutectic point temperature (-60.9 ℃) or the KOH concentration in the unfrozen solution goes above the eutectic point concentration ($x_{KOH} = 0.1367$).[92] To further understand Figure 14, we can make cuts through this diagram at a given temperature or mol% ice (-60 ℃ and 1 mol% ice are shown on Figure 14). Several examples are given in Table 5 and Table 6.

We choose a 30 wt% KOH electrolyte system as an example because the composition provides the maximum ionic conductivity for the single solute system. The mole fraction of additives should not exceed the maximum mole fraction listed in Table 4. Equation (61) and (62) can be used to convert weight percentages of KOH and additive *j* to mole fractions.

$$x_{KOH} = \frac{w_{KOH}/M_{KOH}}{w_{KOH}/M_{KOH} + w_j/M_j + (1 - w_{KOH} - w_j)/M_{H_2O}} \tag{61}$$

$$x_j = \frac{w_j/M_j}{w_{KOH}/M_{KOH} + w_j/M_j + (1 - w_{KOH} - w_j)/M_{H_2O}} \tag{62}$$

where w represents the weight percentage and M represents the molar mass of KOH or additive. Total mole fraction is the sum of the mole fractions of KOH and additive *j*. For three initial compositions: 30 wt% KOH, 15 wt% KOH + 15 wt% K_2CO_3, and 15 wt% KOH + 15 wt% CH_3OH, -60 ℃ is chosen as the given temperature. For initial compositions of 20 wt% KOH + 5% Na_2CO_3 and 20 wt% KOH + 5% K_2HPO_4, T_{given} is the freezing point at the maximum mole fraction in Table 4. The initial total solute mole fraction is shown in Table 5 and Table 6. The mol% ice is calculated based on Equation (60). As is shown in Table 5, for constant given temperature, mol% ice in unconfined electrolytes is higher than for confined electrolytes. Table 6

reveals that the confined electrolytes require more cooling than unconfined electrolytes to obtain the same mol% ice. In other words, a smaller amount of ice formation is expected in the nanoporous environment of zinc electrode and the gas diffusion layers at equilibrium.

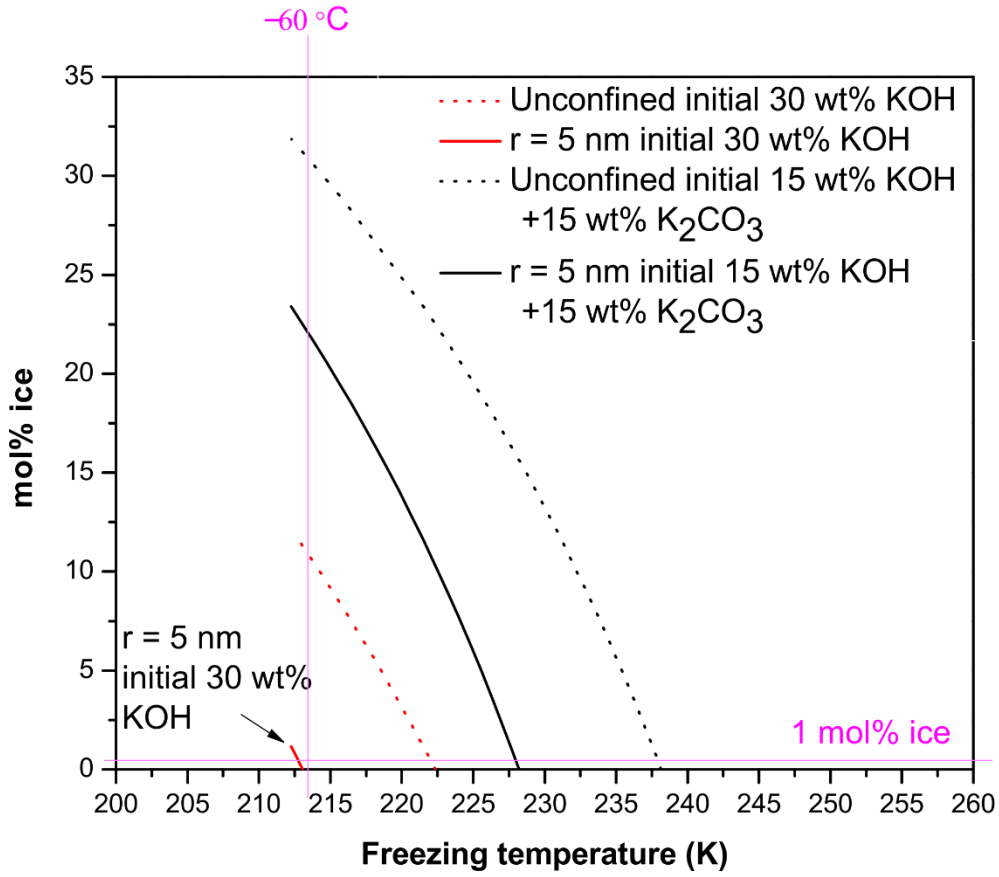

Figure 14. Predicted mol% ice of electrolyte solutions, either unconfined or confined in a pore of $r = 5$ nm, for *i)* an initial wt% KOH of 30% or *ii)* an initial wt% KOH of 15% plus 15 wt% K_2CO_3. For the predictions, $\theta = 0$ and $\sigma^{SL} = 32$ mJ/m^2 are assumed. Cuts through the diagram at -60 ℃ and 1 mol% ice are shown.

Table 5. Mol% ice at the given temperature in the four electrolyte systems.

Electrolytes with initial wt% before freezing	**Initial mol% solute**	**Ratio $\eta = \frac{x_j}{x_{KOH}}$**	**Given temperature T_{given} ($°C$)**	**Mol% ice / mol% unfrozen water @ T_{given}**	
				Unconfined	**$r = 5\ nm$**
30 wt% KOH	12.10%	0	−60 °C	11.21% / 76.69%	0% / 87.90%
15 wt% KOH + 15 wt% K_2CO_3	8.821%	0.4060	−60 °C	31.13% / 60.05%	22.35% / 68.83%
15 wt% KOH + 15 wt% CH_3OH	15.92%	1.751	−60 °C	26.73% / 57.35%	16.98% / 67.10%
20 wt% KOH + 5 wt% Na_2CO_3	8.841%	0.1323	−33.31 °C	3.61% / 87.55%	0% / 91.16%
20 wt% KOH + 5 wt% K_2HPO_4	8.470%	0.08052	−49.71 °C	26.12% / 65.41%	17.47% / 74.06%

Table 6. Freezing temperature to give 1 mol% ice in the four electrolyte systems.

Electrolytes with initial wt% before freezing	**Initial total solute mole fraction x_i**	**Ratio $\eta = \frac{x_j}{x_{KOH}}$**	**Temperature ($°C$) to form 1 mol% ice**	
			Unconfined	**$r = 5\ nm$**
30wt% KOH	0.1210	0	−51.52 °C	−60.78 °C
15 wt% KOH+ 15 wt% K_2CO_3	0.08821	0.4060	−35.52 °C	−45.45 °C
15 wt% KOH+ 15 wt% CH_3OH	0.1592	1.751	−39.74 °C	−49.50 °C
20 wt% KOH+ 5 wt% Na_2CO_3	0.08841	0.1323	−32.03 °C	−42.12 °C
20 wt% KOH+ 5 wt% K_2HPO_4	0.08470	0.08052	−32.62 °C	−40.76 °C

3.5. Conclusions

We studied the effect of solute compositions and nanoscale confinement on the freezing point and equilibrium amount of ice formed under low temperature conditions using our previously published confinement-dependent freezing point equation (Equation (52) and Equation (37) in Chapter 2)[78] and the Elliott *et al.* form of the multisolute osmotic virial equation (Equation (54))[81]. The target electrolytes were KOH-based aqueous systems, which are the most commonly used for large-scale zinc–air batteries in energy grid applications. To keep the technological relevance to practical applications, the additive species we studied were chosen among those that are actively used in the field to improve the performance of the zinc electrode or for other reasons. The osmotic virial equation parameters were tabulated for various electrolytes. Due to the Gibbs–Thomson effect, the freezing point decreased as the radii of pores decreased. When

the ice–solution interface radius of curvature was reduced to the nanoscale, the decrease in freezing point became significant. In other words, confined electrolytes inside the nanopores of the zinc electrodes and the gas diffusion layer will require further undercooling to allow freezing, which suggests a relief to potential clogging or pore collapse problems under low temperature operations of batteries. Our results also emphasized the fact that the additives that improve the performance of zinc electrodes can also have additional effect on the freezing point of the electrolyte system. Such effect was illustrated in our calculations of the amount of ice formed in the electrolyte system based on the lever rule. This thermodynamic method can be further extended to other applications where aqueous solutions are used under nanoscale confinement, such as in water purification membranes, desalination facilities, and organ-on-chip applications.

4. Conclusions

In this thesis, the thermodynamic equilibrium of multicomponent solid–liquid systems with curved solid–liquid interfaces is investigated.

We start by giving a full derivation of the thermal, mechanical, and chemical equilibrium conditions for binary solid–liquid equilibrium, including the effects of radius of curvature of the solid–liquid interface and contact angle that the solid–liquid interface makes with a confining pore wall. This derivation was based on Gibbsian thermodynamics of composite systems together with geometric knowledge of volumes and areas. The derivation yields an equation for the equilibrium temperature as a function of mole fraction and radius of curvature. This

derivation highlights the equivalence of the general forms of the Gibbs–Thomson and Oswald–Freundlich equations.

To show the effect of curvature, we first use the water/glycerol system as an example. A solid–liquid phase diagram was developed over the complete range of concentrations. A curved solid–liquid interface has an effect on both freezing of pure water and precipitation of pure glycerol. This curvature affected phase diagram is compared with the traditional flat interface phase diagram. The freezing point and precipitating point depression increases as the radius of curvature decreases. Nanoscale interface curvature has a significant effect on composition-dependent freezing and precipitating process, eutectic point temperature and concentration. The calculation procedure in this thesis presents a way of combining chemical potential equilibrium with mechanical equilibrium to predict solid–liquid equilibrium in the presence of curved solid–liquid interfaces in multicomponent systems over the complete range of concentration.

Furthermore, the freezing point of the electrolyte is an important issue for operation of aqueous electrolyte batteries in cold climates. We apply the equation for the equilibrium freezing temperature as a function of concentration and interface curvature to investigate the freezing process of electrolytes in zinc–air batteries. We focus on the effect of composition and nanoscale confinement on the freezing of aqueous electrolytes in zinc–air batteries. First, osmotic virial equation parameters are tabulated by fitting literature experimental freezing point data for various electrolytes that are used in zinc–air batteries. Then, we use the parameters to calculate the freezing points of electrolytes with additives with and without nanoscale curvature. There is nanoporous structure on the separator, zinc anode and air cathode, and confinement of electrolyte can be found in these three places. Nanoscale confinement in the zinc–air battery further decreases the freezing point of the electrolyte. When the radius of pores is reduced to the

nanoscale, the decrease in freezing point becomes significant. When the temperature decreases, water will freeze in the bulk unconfined electrolytes, and electrolytes confined inside the nanopores will stay unfrozen until lower temperatures due to the confinement effect. The chosen additives can not only improve battery performance, but also have an effect on the freezing point of the electrolyte system. The effect of the amount of additive is also investigated. When the ratio between mole fraction of KOH and additive increases, the freezing point decreases for unconfined electrolytes and for constant pore size of confinement. The amount of ice formed in zinc–air batteries at a given temperature was calculated based on the lever rule. We plot the mol% ice at a range of temperatures for 4 electrolytes: the combinations of two confinement conditions (unconfined *vs.* pore size r = 5 nm) and two initial solute concentrations (30 wt% KOH *vs.* 15 wt% KOH + 15 wt% K_2CO_3). And we tabulated the mol% ice at a given temperature, and the freezing temperature for 1 mol% ice formation for different electrolytes with additives. The mol% ice formation decreases when the electrolyte is confined.

There are some limitations in this thesis that can be enumerated. First, the Margules parameters used for the water/glycerol system were considered to be independent of temperature. Second, the interfacial tensions between each solid and aqueous liquid solution were taken to be constants, independent of curvature, concentration, and temperature. The equilibrium temperature depression predictions for both unconfined and confined conditions could be made more accurately using the methods described in this thesis if the glycerol solid–liquid interfacial tension were known. Last, we assume that the contact angle that the solid–liquid interface makes with capillary wall is zero.

This thesis gives a promising theoretical method to predict thermodynamic properties of solid–liquid equilibrium across a curved interface in nonideal multicomponent systems (binary system

of water/glycerol system in Chapter 2 and multicomponent case in Chapter 3). And has applications in many fields such as cryobiology, forestry, soil science, nanoporous materials and low temperature battery design.

References

(1) Elliott, J. A. W. On the Complete Kelvin Equation. *Chem.Eng.Educ* **2001**, 35, 274–278.

(2) Ge, S.; Wang, C. Y. Characteristics of Subzero Startup and Water/ice Formation on the Catalyst Layer in a Polymer Electrolyte Fuel Cell. *Electrochim. Acta* **2007**, *52* (14), 4825–4835.

(3) Thomson, S. W. On the Equilibrium of Vapour at a Curved Surface of Liquid. *Proc. R. Soc. L.* **1872**, *7*, 63–68.

(4) Melrose, J. C. Model Calculations for Capillary Condensation. *AIChE J.* **1966**, *12* (5), 986–994.

(5) Gibbs, J. W. On the Equilibrium of Heterogeneous Substances. *Am. J. Sci* **1878**, s3−16, 441−458.

(6) Fisher, L. R.; Israelachvili, J. N. Direct Experimental Verification of the Kelvin Equation for Capillary Condensation. *Nature*. **1979**, *227*, 548–549.

(7) Fisher, R.; Israelachvili, J. N. Experimental Studies on the Applicability of the Kelvin Equation to Highly Curved Concave Menisci. *J. Colloid Interface Sci.* **1981**, *80* (2), 528–541.

(8) Shapiro, A. A.; Stenby, E. H. Kelvin Equation for a Non-Ideal Multicomponent Mixture. *Fluid Phase Equilib.* **1997**, *134*, 87–101.

(9) Ward, C. A.; Balakrishnan, A.; Hooper, F. C. On the Thermodynamics of Nucleation in Weak Gas–Liquid Solutions. *J. Basic Eng.* **1970**, *92* (10), 695–704.

(10) Shapiro, A. A.; Stenby, E. H. Thermodynamics of the Multicomponent Vapor–Liquid Equilibrium under Capillary Pressure Difference. *Fluid Phase Equilib.* **2001**, *178* (1), 17–32.

(11) Eslami, F.; Elliott, J. A. W. Design of Microdrop Concentrating Processes. *J. Phys. Chem. B* **2013**, *117* (7), 2205–2214.

(12) Eslami, F.; Elliott, J. A. W. Stability Analysis of Microdrops during Concentrating

Processes. *J. Phys. Chem. B* **2014**, *118* (13), 3630–3641.

(13) Webber, J. B. W. Studies of Nano-Structured Liquids in Confined Geometries and at Surfaces. *Prog. Nucl. Magn. Reson. Spectrosc.* **2010**, *56* (1), 78–93.

(14) Liu, Z.; Muldrew, K.; Wan, R. G.; Elliott, J. A. W. Measurement of Freezing Point Depression of Water in Glass Capillaries and the Associated Ice Front Shape. *Phys. Rev. E* **2003**, *67*, 61602.

(15) Christenson, H. K. Confinement Effects on Freezing and Melting. *J. Phys.: Condens. Matter* **2001**, *13*, R95–R133.

(16) Findenegg, G. H.; Jähnert, S.; Akcakayiran, D.; Schreiber, A. Freezing and Melting of Water Confined in Silica Nanopores. *ChemPhysChem* **2008**, *9* (18), 2651–2659.

(17) Fagerlund, G. Determination of Pore-Size Distribution from Freezing-Point Depression. *Mater. Constr.* **1973**, *6* (3), 215–225.

(18) Hirama, Y.; Takahashi, T.; Hino, M.; Sato, T. Studies of Water Adsorbed in Porous Vycor Glass. *J. Colloid Interface Sci.* **1996**, *184* (2), 349–359.

(19) Ashworth, E. N.; Abeles, F. B. Freezing Behavior of Water in Small Pores and the Possible Role in the Freezing of Plant Tissues. *Plant Physiol.* **1984**, *76* (1), 201–204.

(20) Mazur, P. The Role of Cell Membranes in the Freezing of Yeast and Other Single Cells. *Ann. N. Y. Acad. Sci.* **1965**, *125*, 658–676.

(21) Acker, J. P.; Elliott, J. A. W.; McGann, L. E. Intercellular Ice Propagation: Experimental Evidence for Ice Growth Through Membrane Pores. *Biophys. J.* **2001**, *81*, 1389–1397.

(22) Jacot, A.; Rappaz, M. A Pseudo-Front Tracking Technique for the Modelling of Solidi Cation Microstructures in Multi-Component Alloys. *Acta Mater.* **2002**, *50*, 1909–1926.

(23) Ostwald, W. On the Assumed Isomerism of Red and Yellow Mercury Oxide and the Surface-Tension of Solid Bodies. *Z. Phys. Chem.* **1900**, *34*, 495.

(24) Freundlich H. Kapillarchemie. *Akademische Verlagsgesellschaft*. **1922**.

(25) Defay, R. *Surface Tension and Adsorption*, English ed.; Longmans: London, England,

1966.

(26) Freundlich, H. *Colloid and Capillary Chemistry*; E. P. Dutton and Company: New York, 1923.

(27) Eslami, F.; Elliott, J. A. W. Role of Precipitating Solute Curvature on Microdrops and Nanodrops during Concentrating Processes: The Nonideal Ostwald−Freundlich Equation. *J. Phys. Chem. B* **2014**, 118, 14675−14686.

(28) Tan, S. P.; Piri, M. Equation-of-State Modeling of Associating-Fluids Phase Equilibria in Nanopores. *Fluid Phase Equilib.* **2015**, *405*, 157–166.

(29) Shardt, N.; Elliott, J. A. W. Thermodynamic Study of the Role of Interface Curvature on Multicomponent Vapor-Liquid Phase Equilibrium. *J. Phys. Chem. A* **2016**, *120* (14), 2194–2200.

(30) Tan, S. P.; Piri, M. Equation-of-State Modeling of Confined-Fluid Phase Equilibria in Nanopores. *Fluid Phase Equilib.* **2015**, *393*, 48–63.

(31) Tanaka, T.; Hara, S.; Cermak. Thermodynamic Evaluation of Binary Phase Diagram of Small Particle Systems. *Z.Metallkd.* **2001**, *92*, 467–472.

(32) Jesser, W. A.; Shneck, R. Z.; Gile, W. W. Solid−Liquid Equilibria in Nanoparticles of Pb-Bi Alloys. *Phys. Rev. B* **2004**, *69* (14), 1–13.

(33) Seiler, M.; Groß, J.; Bungert, B.; Sadowski, G.; Arlt, W. Modeling of Solid/Fluid Phase Equilibria in Multicomponent Systems at High Pressure. *Chem. Eng. Technol.* **2001**, *24* (6), 607–612.

(34) Walas, S. M. *Phase Equilibria in Chemical Engineering*; Butterworth: Boston, MA, 1985.

(35) Miner, C.; Dalton, N. Glycerine: An Overview. *Chem. Soc. Monogr.* **1953**, *117* (212), 1–27.

(36) Polge, C.; Smith, A. U.; Parkes, A. S. Revival of Spermatozoa after Vitrification and Dehydration at Low Temperatures. *Nature*. **1949**, *164*, 666.

(37) Callen, H. B. *Thermodynamics and an Introduction to Thermostatistics*, 2nd Ed., John

Wiley & Sons: New York, 1985.

(38) Polyanin, A. D; Manzhirov, A. V. *Handbook of Mathematics for Engineers and Scientists*; CRC Press, 2006.

(39) Elliott, J. A. W.; Prickett, R. C.; Elmoazzen, H. Y.; Porter, K. R.; McGann, L. E. A Multisolute Osmotic Virial Equation for Solutions of Interest in Biology. *J. Phys. Chem. B* **2007**, 111, 1775–1785.

(40) Prickett, R. C.; Elliott, J. A. W.; McGann, L. E. Application of the Osmotic Virial Equation in Cryobiology. *Cryobiology* **2010**, *60* (1), 30–42.

(41) Elliott, J. R.; Lira, C. T. *Introductory Chemical Engineering Thermodynamics*, 2nd ed.; Prentice-Hall Inc: Upper Saddle River: New York, 2012; pp450.

(42) Zielinski, M. W.; McGann, L. E.; Nychka, J. A.; Elliott, J. A. W. Comparison of Non-Ideal Solution Theories for Multi-Solute Solutions in Cryobiology and Tabulation of Required Coefficients. *Cryobiology* **2014**, *69*, 305–317.

(43) Du, Y. J; Yen, T. T; Chen, L. R. Theoretical Calculation of the Mole Fraction at the Eutectic Point for a Binary System. *Phys. Stat. Soli B* **1985**, 130 (1), K5–K10.

(44) Olawale, M.; Amuda, H.; Akabekwa, R. O. Estimating the Eutectic Composition of Simple Binary Alloy System Using Linear Geometry. *Leonardo J. Sci.* **2008**, *12*, 232–242.

(45) Htira, T.; Cogné, C.; Gagnière, E.; Mangin, D. Determination of the Solid–Liquid Phase Diagram of the Binary System Propionic Acid/Water. *J. Chem. Eng. Data* **2016**, *61* (2), 806–812.

(46) *CRC Handbook of Chemistry and Physics*; Knovel: Binghamton, NY, 2017.

(47) Zargarzadeh. L.; Elliott, J. A. W. Comparison of the Osmotic Virial Equation with the Margules Activity Model and Their Application to Solid–liquid Equilibrium. **2017**, to be submitted.

(48) Prausnitz, J. M.; Lichtenthaler, R. N.; Azevedo, E. G. D. *Molecular Thermodynamics of Fluid-Phase Equilibria*, 3rd ed.; Pearson Education, 1998.

(49) Lane, L. B. Freezing Points of Glycerol and Its Aqueous Solutions. *Ind. Eng. Chem.* **1925**, *17*, 924.

(50) Takamura, K.; Fischer, H.; Morrow, N. R. Physical Properties of Aqueous Glycerol Solutions. *J. Pet. Sci. Eng.* **2012**, *98–99*, 50–60.

(51) Binks, B. P.; Clint, J. H. Solid Wettability from Surface Energy Components: Relevance to Pickering Emulsions. *Langmuir* **2002**, *18* (4), 1270–1273.

(52) Hillig, W. B. Measurement of Interfacial Free Energy for Ice/water System. *J. Cryst. Growth* **1998**, *183* (3), 463–468.

(53) Han, B.; Bischof, J. C. Direct Cell Injury Associated with Eutectic Crystallization during Freezing. *Cryobiology* **2004**, *48* (1), 8–21.

(54) Peppin, S. S. L.; Style, R. W. The Physics of Frost Heave and Ice-Lens Growth. *Vadose Zo. J.* **2013**, *12*, 1.

(55) Jackson, K. A.; Chalmers, B. Freezing of Liquids in Porous Media with Special Reference to Frost Heave in Soils. *J. Appl. Phys.* **1958**, *29* (8), 1178–1181.

(56) Neufeld, R. et al., *Powering Canada's Territories;* Technical Report for Standing Senate Committee on Energy, the Environment and Natural Resources: Canada, 2014.

(57) Rahman, A.; Wang, X.; Wen, C. High Energy Density Metal–Air Batteries : A Review. *J. Electrochem. Soc*. **2013**, *160* (10), A1759–A1771.

(58) Koscher, G.; Kordesch, K. Can Refillable Alkaline Methanol–Air Systems Replace Metal –Air Cells? *J. Power Sources.* **2004**, *136* (2), 215–219.

(59) Lee, J.; Kim, S. T.; Cao, R.; Choi, N.; Liu, M.; Lee, K. T. Metal–Air Batteries with High Energy Density: Li–Air versus Zn–Air. *Adv. Energy Mater.* **2011**, *1* (1), 34–50.

(60) Wang, Y.; Zhou, H. A Lithium–Air Fuel Cell Using Copper to Catalyze Oxygen-Reduction Based on Copper-Corrosion Mechanism W. *Chem. Commun.* **2010**, 6305–6307.

(61) Wang, Y.; Zhou, H. A Lithium–Air Battery with a Potential to Continuously Reduce O_2 from Air for Delivering Energy. *J. Power Sources*. **2010**, *195* (1), 358–361.

(62) Sathyanarayana, S.; Munichandraiah, N. A New Magnesium–Air Cell for Long-Life Applications. *J. Appl. Electrochem.* **1981**, *11* (1), 33–39.

(63) Linden, D.; Reddy, T. B. *Handbook of Batteries*, 3rd ed.; McGraw-Hill: New York, 2002.

(64) Yang, S. Design and Analysis of Aluminum/air Battery System for Electric Vehicles. *J. Power Sources* **2002**, *112* (1), 162–173.

(65) Khan, P. A.; Venkatesh, B. Economic Analysis of Chemical Energy Storage Technologies. *SmartCity 360 2016, SmartCity 360 2015.* Lecture Notes of the Institute for Computer Sciences, Social Informatics and Telecommunications Engineering, Springer, Cham, **2016**; pp 277–291.

(66) Fu, J.; Cano, Z. P.; Park, M. G.; Yu, A.; Fowler, M.; Chen, Z. Electrically Rechargeable Zinc–Air Batteries: Progress, Challenges, and Perspectives. *Adv. Mater.* **2017**, *29* (7), 1604685.

(67) Chakkaravarthy, C.; Waheed, A. K. A.; Udupa, H. V. K. Zinc–Air Alkaline Batteries—A Review. *J. Power Sources* **1981**, *6* (3), 203–228.

(68) McLarnon, F. R. Cairns, E. J. The Secondary Alkaline Zinc Electrode. *J. Electrochem. Soc.* **1991**, *138* (2), 645–646.

(69) Gilliam, R. J.; Graydon, J. W.; Kirk, D. W.; Thorpe, S. J. A Review of Specific Conductivities of Potassium Hydroxide Solutions for Various Concentrations and Temperatures. *Int. J. Hydrog. Energy.* **2007**, *32*, 359–364.

(70) Sapkota, P.; Kim, H. An Experimental Study on the Performance of a Zinc Air Fuel Cell with Inexpensive Metal Oxide Catalysts and Porous Organic Polymer Separators. *J. Ind. Eng. Chem.* **2010**, *16* (1), 39–44.

(71) Diggle, J. W.; Despic, A. R.; Bockris, J. O. M. The Mechanism of the Dendritic Electrocrystallization of Zinc. *J. Electrochem. Soc.* **1967**, *116* (11), 1503–1514.

(72) Despić, A. R.; Purenović, M. M. Critical Overpotential and Induction Time of Dendritic Growth. *J. Electrochem. Soc.* **1974**, *121* (3), 329–335.

(73) Wang, R. Y.; Kirk, D. W.; Zhang, G. X. Effects of Deposition Conditions on the

Morphology of Zinc Deposits from Alkaline Zincate Solutions. *J. Electrochem. Soc.* **2006**, *153* (5), C357–C364.

(74) Simičić, M. V.; Popov, K. I.; Krstajić, N. V. An Experimental Study of Zinc Morphology in Alkaline Electrolyte at Low Direct and Pulsating Overpotentials. *J. Electroanal. Chem.* **2000**, *484* (1), 18–23.

(75) Mainar, A. R.; Leonet, O.; Bengoechea, Miguel, et al. Alkaline Aqueous Electrolytes for Secondary Zinc–air Batteries: An Overview. *Int. J. Energy Res.* **2016**, *40* (8), 1032–1049.

(76) Xu, M.; Ivey, D. G.; Xie, Z.; Qu, W. Rechargeable Zn–Air Batteries: Progress in Electrolyte Development and Cell Configuration Advancement. *J. Power Sources.* **2015**, *283*, 358–371.

(77) Chamoun, M.; Hertzberg, B. J.; Gupta, T.; Davies, D.; Bhadra, S.; Tassell, B. V; Erdonmez, C.; Steingart, D. A. Hyper-Dendritic Nanoporous Zinc Foam Anodes. *NPG Asia Mater.* **2015**, *7*, e178.

(78) Liu, F; Zargarzadeh, L; Chung, H. J; Elliott, J. A. W. Thermodynamic Investigation of the Effect of Interface Curvature on Solid–Liquid Equilibrium and Eutectic Point of Binary Mixture. *J. Phys. Chem. B*. **2017**, *121* (40), 9452–9462.

(79) Haynes, W. M. CRC Handbook of Chemistry and Physics, 95th Edition; CRC Press: Boca Raton, Florida, 2014.

(80) Prickett, R. C.; Elliott, J. A. W.; McGann, L. E. Application of the Multisolute Osmotic Virial Equation to Solutions Containing Electrolytes. *J. Phys. Chem. B.* **2011**, *115* (49), 14531–14543.

(81) Prickett, R. C.; Elliott, J. A. W.; McGann, L. E. Application of the Osmotic Virial Equation in Cryobiology. *Cryobiology* **2010**, *60* (1), 30–42.

(82) Elliott, J. A. W.; Prickett, R. C.; Elmoazzen, H. Y.; Porter, K. R.; McGann, L. E. A Multisolute Osmotic Virial Equation for Solutions of Interest in Biology. *J. Phys. Chem. B*. **2007**, *111* (7), 1775–1785.

(83) Bro, P.; Kang, H. Y. The Low-Temperature Activity of Water in Concentrated KOH Solutions. *J. Electrochem. Soc.* **1971**, *118* (9), 1430.

(84) Adler, T. C.; McLarnon, F. R.; Cairns, E. J. Investigations of a New Family of Alkaline−Fluoride−Carbonate Electrolytes for Zinc/Nickel Oxide Cells. *Ind. Eng. Chem. Res.* **1998**, *37* (8), 3237–3241.

(85) Jindra, J. Progress in Sealed Ni–Zn Cells, 1991–1995. *J. Power Sources* **1997**, *66* (1–2), 15–25.

(86) Thornton, R. F. Properties of Alternate Electrolytes for Secondary Zinc Batteries. *J. Electrochem. Soc.* **1980**, *127* (7), 1448–1452.

(87) Lee, C. W.; Sathiyanarayanan, K.; Eom, S. W.; Kim, H. S.; Yun, M. S. Novel Electrochemical Behavior of Zinc Anodes in Zinc/air Batteries in the Presence of Additives. *J. Power Sources* **2006**, *159* (2), 1474–1477.

(88) Lan, C. J.; Lee, C. Y.; Chin, T. S. Tetra-Alkyl Ammonium Hydroxides as Inhibitors of Zn Dendrite in Zn-Based Secondary Batteries. **2007**, *52*, 5407–5416.

(89) Schröder, D.; Sinai Borker, N. N.; König, M.; Krewer, U. Performance of Zinc Air Batteries with Added K_2CO_3 in the Alkaline Electrolyte. *J. Appl. Electrochem.* **2015**, *45* (5), 427–437.

(90) Jost, E. M. Nickel–zinc Battery System Having an Aqueous Electrolyte Consisting of Potassium Hydroxide and Potassium Carbonate. U.S. Patent 3,485,673, Dec. 23, 1969.

(91) Ko, H. W.; Juang, H. K. Absorption of CO_2 by Alkaline Electrolyte and Its Effect on Electrical Discharge. *J. Appl. Electrochem.* **1983**, *13* (6), 725–730.

(92) Grant, S. A.; Baker, J. M.; Iskandar, I. K. *Contaminant Hydrology: Cold Regions Modeling*; CRC Press, 2000.